

---

This is an electronic reprint of the original article.  
This reprint may differ from the original in pagination and typographic detail.

Kang, Running; Wang, Xuehai; Huang, Junqin; An, Sufeng; Wang, Lu; Wang, Gang; Chen, Hong; Zhang, Cuijuan; Bin, Feng; Li, Yongdan

## Distinct structure-activity relationship and reaction mechanism over BaCoO<sub>3</sub>/CeO<sub>2</sub> catalysts for NO direct decomposition

*Published in:*  
Applied Catalysis B: Environmental

*DOI:*  
[10.1016/j.apcatb.2024.123952](https://doi.org/10.1016/j.apcatb.2024.123952)

Published: 05/08/2024

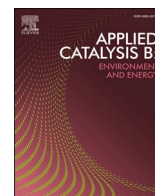
*Document Version*  
Publisher's PDF, also known as Version of record

*Published under the following license:*  
CC BY

*Please cite the original version:*  
Kang, R., Wang, X., Huang, J., An, S., Wang, L., Wang, G., Chen, H., Zhang, C., Bin, F., & Li, Y. (2024). Distinct structure-activity relationship and reaction mechanism over BaCoO<sub>3</sub>/CeO<sub>2</sub> catalysts for NO direct decomposition. *Applied Catalysis B: Environmental*, 350, Article 123952. <sup>2</sup>  
<https://doi.org/10.1016/j.apcatb.2024.123952>

---

This material is protected by copyright and other intellectual property rights, and duplication or sale of all or part of any of the repository collections is not permitted, except that material may be duplicated by you for your research use or educational purposes in electronic or print form. You must obtain permission for any other use. Electronic or print copies may not be offered, whether for sale or otherwise to anyone who is not an authorised user.



## Distinct structure-activity relationship and reaction mechanism over BaCoO<sub>3</sub>/CeO<sub>2</sub> catalysts for NO direct decomposition

Running Kang<sup>a,b,c</sup>, Xuehai Wang<sup>d</sup>, Junqin Huang<sup>b,c</sup>, Sufeng An<sup>d</sup>, Lu Wang<sup>a</sup>, Gang Wang<sup>d,\*</sup>, Hong Chen<sup>e</sup>, Cuijuan Zhang<sup>f</sup>, Feng Bin<sup>b,c,\*\*</sup>, Yongdan Li<sup>a,\*</sup>

<sup>a</sup> Department of Chemical and Metallurgical Engineering, School of Chemical Engineering, Aalto University, Kemistintie 1, Espoo, P.O. Box 16100, FI-00076, Finland

<sup>b</sup> State Key Laboratory of High-Temperature Gas Dynamics, Institute of Mechanics, Chinese Academy of Sciences, Beijing 100190, China

<sup>c</sup> School of Engineering Science, University of Chinese Academy of Sciences, Beijing 100049, China

<sup>d</sup> Dalian Research Institute of Petroleum and Petrochemicals, SINOPEC, Dalian 116045, China

<sup>e</sup> School of Environmental Science & Engineering, Tianjin University, Tianjin 300072, China

<sup>f</sup> Collaborative Innovation Center of Chemical Science and Engineering (Tianjin), Tianjin Key Laboratory of Applied Catalysis Science and Technology, State Key Laboratory of Chemical Engineering (Tianjin University), School of Chemical Engineering and Technology, Tianjin University, Tianjin 300072, China

### ARTICLE INFO

#### Keywords:

NO direct decomposition  
Perovskite  
BaCoO<sub>3</sub>  
CeO<sub>2</sub> morphology  
Reaction mechanism

### ABSTRACT

The dependency on morphology is crucial for achieving highly efficient direct decomposition of NO. Herein, a BaCoO<sub>3</sub>/CeO<sub>2</sub> catalyst is synthesized using CeO<sub>2</sub> small particles (p), spheres (s) and rods (r) as supports. The NO conversion to N<sub>2</sub> (NTN<sub>2</sub>) at 800 °C follows the order BaCoO<sub>3</sub>/CeO<sub>2</sub>-r (78.8 %) > BaCoO<sub>3</sub>/CeO<sub>2</sub>-s (75.9 %) > BaCoO<sub>3</sub>/CeO<sub>2</sub>-p (56.9 %) > BaCoO<sub>3</sub> (8.6 %) at a space velocity 1 g s/cm<sup>3</sup>. BaCoO<sub>3</sub>/CeO<sub>2</sub>-r exhibits high tolerance to O<sub>2</sub> and stability with conversion decreasing from 78.8 % to 74.6 %, 60.0 % and 50.0 % at 800 °C with 1, 5 and 10 vol% O<sub>2</sub>, respectively. The high redox activity, higher active oxygen mobility and NO adsorption capability ensures its superior performance, while the high surface area (31.29 m<sup>2</sup>/g) and uniform distribution of active sites on the surface further promote the activity. The mechanism of NO direct decomposition is elucidated by *in situ* Diffuse reflectance infrared Fourier transform spectroscopy, <sup>18</sup>O<sub>2</sub> isotopic transient exchange experiments and density functional theory (DFT) calculation.

### 1. Introduction

Nitrogen oxides (NO<sub>x</sub>), emitted in the flue gas of the industrial furnace such as new-type dry cement production process (800 °C) and gasification cooling stack in steelmaking (750–800 °C), are extremely toxic to human health and environment via forming acid rain, photochemical smog, and ozone layer depletion [1]. Currently, several technologies have been proposed for NO<sub>x</sub> abatement, including selective catalytic reduction (SCR) with ammonia, selective non-catalytic reduction and NO<sub>x</sub> storage and reduction, etc. [2–8]. Among these technologies, NO direct decomposition (2NO → N<sub>2</sub> + O<sub>2</sub>) has been regarded as the most appealing pathway for NO removal due to its eco-friendly and no requirement of reductants [9]. The NO direct decomposition reaction possesses thermodynamic feasibility but belongs to a slow kinetic reaction with high activation energy (~335 kJ/mol) [10]. Therefore, the development of high-performance catalyst for NO elimination and the

elucidation of the reaction mechanism are imperative.

Transition metal oxides, rare earth metal oxides, zeolites, and perovskite catalysts have been explored for NO direct decomposition [11–14]. Recently perovskite structured oxides have been investigated in many works [15]. Xu et al. reported that BaCoO<sub>3</sub>, BaMnO<sub>3</sub> and BaFeO<sub>3</sub> perovskite catalysts achieve NO conversion to N<sub>2</sub> (NTN<sub>2</sub>) of 29.2 %, 28.7 % and 24.9 % at 650 °C (1 g s/cm<sup>3</sup>), respectively [16]. CeO<sub>2</sub>, owing to its outstanding redox activity, oxygen storage-release capability and resistance to sintering, has been widely used as one catalyst component in the three-way catalyst, etc. [17,18]. The effect of BaCoO<sub>3</sub> content on the activity and the interaction between BaCoO<sub>3</sub> and CeO<sub>2</sub> in a sample xBaCoO<sub>3</sub>-CeO<sub>2</sub> synthesized with a citric acid-nitrate one-pot method was examined in our previous work. The NTN<sub>2</sub> of the 5 %BaCoO<sub>3</sub>-CeO<sub>2</sub> sample is 70.1 % while that of BaCoO<sub>3</sub> is 27.2 % at 750 °C (1.5 g s/cm<sup>3</sup>) [19]. The 5 %BaCoO<sub>3</sub>-CeO<sub>2</sub> sample remains NTN<sub>2</sub> 71.1 % at 800 °C in the presence of 1 vol% O<sub>2</sub>. In BaCoO<sub>3</sub>-CeO<sub>2</sub> sample,

\* Corresponding authors.

\*\* Corresponding author at: State Key Laboratory of High-Temperature Gas Dynamics, Institute of Mechanics, Chinese Academy of Sciences, Beijing 100190, China.

E-mail addresses: [wanggang.fshy@sinopec.com](mailto:wanggang.fshy@sinopec.com) (G. Wang), [binfeng@imech.ac.cn](mailto:binfeng@imech.ac.cn) (F. Bin), [yongdan.li@aalto.fi](mailto:yongdan.li@aalto.fi) (Y. Li).

BaCoO<sub>3</sub> is proved as the primary active sites to adsorb NO, while CeO<sub>2</sub> improves the reducibility, oxygen mobility and sintering resistance [20]. The morphology of CeO<sub>2</sub> was demonstrated to influence the metal active site dispersion and induce a strong metal-support interaction (MSI) with an appropriate morphology [18,21]. But the intrinsic structure-activity relationship (morphology, reaction interface, oxygen vacancy, etc.) over BaCoO<sub>3</sub> loading on different morphology of CeO<sub>2</sub> are still lacking for NO direct decomposition reaction.

For the mechanism of NO direct decomposition on the perovskite-type catalyst, Shin et al. [22] proposed that two NO molecules attack active sites and oxygen vacancies simultaneously and nitrosyl species (NO<sup>•</sup>) form and adsorb on iron ion to form N<sub>2</sub> and O<sub>2</sub> over SrFeO<sub>3-x</sub> catalyst. Teraoka et al. assumed that the attacking of two NO molecules in the adjacent oxide ion vacancies happens successively on a La<sub>0.4</sub>Sr<sub>0.6</sub>Mn<sub>0.8</sub>Ni<sub>0.2</sub>O<sub>3</sub> catalyst and the reaction follows the first-order law [23]. Chen et al. guessed that two adsorbed NO\* dissociate to produce N<sub>2</sub> firstly, and NO\* reacts with surface oxygen to form a NO<sub>2</sub> intermediate, which decomposes rapidly to produce NO and O<sub>2</sub> over a La<sub>1.6</sub>Ba<sub>0.4</sub>NiO<sub>4</sub> catalyst [24]. Recently, Xie et al. thought that NO adsorption on the metal site near oxygen vacancy to form N<sub>2</sub>O\* and O\* is the rate determining step (RDS) on a BaCoO<sub>3</sub>-CeO<sub>2</sub> catalyst [21]. However, so far, there is no direct evidence to elucidate its reaction mechanism for NO direct decomposition, particularly the roles of different intermediates on the perovskite-type catalysts.

Herein, a series of CeO<sub>2</sub> with varying morphologies, i.e., irregular CeO<sub>2</sub> particles (CeO<sub>2</sub>-p), CeO<sub>2</sub> spheres (CeO<sub>2</sub>-s) and CeO<sub>2</sub> rods (CeO<sub>2</sub>-r), were prepared and employed as the supports in a BaCoO<sub>3</sub>/CeO<sub>2</sub> catalyst. The distinct structure-activity relationships of the catalysts were identified. The nature of reaction mechanisms with/without O<sub>2</sub> was investigated with *in-situ* DRIFT, isotopic (<sup>18</sup>O<sub>2</sub>) transient exchange experiment and DFT calculation. The results obtained comprehensively elucidate the effect of CeO<sub>2</sub> morphology on the catalytic activity.

## 2. Experimental

### 2.1. Sample preparation

The BaCoO<sub>3</sub>/CeO<sub>2</sub> catalyst samples were prepared with an excess impregnation method. The irregular CeO<sub>2</sub> particles (CeO<sub>2</sub>-p) was prepared with direct thermal decomposition of Ce(NO<sub>3</sub>)<sub>3</sub>·6H<sub>2</sub>O at 600 °C. Both the nano-sphere (CeO<sub>2</sub>-s) and nano-rod (CeO<sub>2</sub>-r) ceria samples were synthesized with a hydrothermal technique and supplied by Liaoning KeLong Fine Chemical Co., LTD, China. The prescribed amounts of Ba(NO<sub>3</sub>)<sub>2</sub> and Co(NO<sub>3</sub>)<sub>2</sub>·6H<sub>2</sub>O were dissolved in distilled water, and suitable amount of citric acid was added to the solution. The mole ratio of Ba: Co: citric acid is 1:1:1.5. the solution was stirred continuously at 80 °C and the CeO<sub>2</sub> support was immersed to achieve a loading of 5 wt% BaCoO<sub>3</sub>. The reason for choosing BaCoO<sub>3</sub> with a mass ratio of 5 % in all samples is that the 5 %BaCoO<sub>3</sub>-CeO<sub>2</sub> catalyst exhibit the best NO decomposition activity of all catalysts with the loading content of BaCoO<sub>3</sub> from 3–100 wt% in our previous work [19]. Then it was dried at 110 °C for 12 h and calcined at 400 °C for 1 h and 700 °C for 5 h. The samples are referred to as BaCoO<sub>3</sub>/CeO<sub>2</sub>-p (BCP), BaCoO<sub>3</sub>/CeO<sub>2</sub>-s (BCS), and BaCoO<sub>3</sub>/CeO<sub>2</sub>-r (BCR). A BaCoO<sub>3</sub> sample was also prepared with the dissolution of Ba(NO<sub>3</sub>)<sub>2</sub>, Co(NO<sub>3</sub>)<sub>2</sub>·6 H<sub>2</sub>O and suitable amount of citric acid in distilled water. The solution was stirred and evaporated at 80 °C to form a gel, followed by drying at 110 °C for 12 h and calcined at 400 °C for 1 h and then at 700 °C for 5 h.

### 2.2. Characterization

The X-ray diffraction (XRD) patterns were recorded with a X'PERT PRO MPD Alpha1 diffractometer at 40 mA and 45 kV with a Cu K<sub>α</sub> radiation source (λ = 0.154056 nm). Raman spectrum was carried out to obtain oxygen vacancy information on DXR (American Thermo Electron) with a 532 nm laser. The specific surface area (SSA) was measured

using a BEL sorp Mini II instrument. N<sub>2</sub> physisorption isotherms were acquired at -196 °C after outgassing at 250 °C for 3 h under vacuum. The morphology and elemental distribution were observed with a high-resolution transmission electron microscope (HRTEM, JEM 2100F, Oxford) equipped with energy dispersive X-ray detector (EDX) mapping (Tecna G<sup>2</sup> F20, Oxford) and a scanning electron microscope (SEM, Hitachi S-4800). X-ray photoelectron spectroscopy measurement (XPS) was carried out with a Kratos Axis Ultra DLD spectrometer. The binding energy was calibrated with the C1s peak at 284.8 eV.

H<sub>2</sub> temperature-programmed reduction (H<sub>2</sub>-TPR) was performed on an Ichem700 apparatus. The sample (50 mg) was pretreated at 500 °C for 1 h under Ar flow (30 mL/min) to remove adsorbed impurities, and then cooled down to room temperature (RT). The sample was then heated from RT to 900 °C at 10 °C/min with a flow of 5 vol% H<sub>2</sub>/Ar (30 mL/min). Temperature-programmed desorption of O<sub>2</sub> (O<sub>2</sub>-TPD, Ichem700), and NO (NO-TPD-Mass spectrometer, MS, Pfeiffer Omnistar™) were done to examine the chemisorption of O<sub>2</sub> and NO, respectively. For O<sub>2</sub>-TPD, the sample was pretreated at 500 °C for 1 h under Ar flow (30 mL/min) and exposed to O<sub>2</sub> (30 mL/min) for 1 h at RT, followed by operating from RT to 900 °C at 10 °C/min with pure Ar (30 mL/min) after purging with Ar (30 mL/min) for 0.5 h. For NO-TPD-MS, after being pretreated at 700 °C under Ar (50 mL/min) for 1 h, the sample (200 mg) was cooled to 80 °C and then adsorbed to saturation with 2 vol% NO/Ar for 1 h. The desorption gases were recorded with the MS from 80 °C to 700 °C at 10 °C/min.

*In-situ* Diffuse reflectance infrared Fourier transform (DRIFT) spectra were obtained with a Thermo Fisher Scientific Nicolet iS50 spectrometer. The catalyst was pretreated in helium atmosphere with a flow rate of 50 mL/min at 600 °C for 1 h and then cooled to RT. The background spectra were collected at desired temperatures during the cooling process. Afterwards, the reaction gases of 1 vol% NO/He, and 1 vol% NO+2 vol% O<sub>2</sub>/He were switched into the *in-situ* reaction cell with 30 mL/min for 0.5 h until stability, respectively. The steady state spectra were recorded with accumulating 32 scans at 30, 200, 300, 400, 500, 550 and 600 °C, respectively. The isotopic (<sup>18</sup>O<sub>2</sub>) exchange experiments were carried out in an *in-situ* fixed-bed reactor (i.d. = 3 mm), and the products were monitored with an online mass spectrometer (MS, Pfeiffer Omnistar™). A four-way switch valve was firstly used to switch the gas path instantaneously and retain steady continuous flow of reactant gases, as shown in Fig. S1 in the [supporting information](#). The sample (65 mg, 0.09–0.15 mm) was pretreated at 800 °C for about 20 min at the flow rate of 30 mL/min in Ar. Afterwards, the pre-mixed reactant gas (30 mL/min, 1 vol% NO/Ar) was constantly introduced into the reactor at 800 °C for 20 min and the products were monitored with the online MS. Pure Ar was used to purge at 30 mL/min for 10 min to remove the gases. Finally, the mixed reactant gas (30 mL/min, 1 vol% NO + 1 vol% <sup>18</sup>O<sub>2</sub>/Ar) was pulsed into the reactor at 800 °C for about 25 min to detect the isotopic products adequately. The isotopic gas (<sup>18</sup>O<sub>2</sub>) was supplied by WUHAN NEWRADAR SPECIAL GAS Co., LTD.

The density functional theory (DFT) simulation was further performed to clarify the perovskite-support interaction and reaction pathways, and the detailed calculation method was introduced in the [supporting information](#).

### 2.3. Catalytic activity

The catalyst samples (0.5 g, 35–45 mesh) were placed in a fix-bed quartz tube reactor (i.d. = 6 mm). The sample was pretreated to remove the gaseous impurities on the surface at 500 °C for 0.5 h in Ar (30 mL/min) and cool down to RT. 8000 ppm NO/Ar was introduced into the reactor at atmospheric pressure with a flow rate 30 mL/min (1 g s/cm<sup>3</sup>, GHSV=5600 h<sup>-1</sup>). Each temperature step was maintained for 20 min to reach steady state from 500 to 800 °C with an interval of 50 °C. The N<sub>2</sub> concentration was quantified online with the same MS calibrated with an internal standard method. The concentrations of NO, O<sub>2</sub>, CO<sub>2</sub> and SO<sub>2</sub> were measured by online multicomponent analyzers (Gasboard-

300UV for NO/O<sub>2</sub>, Gasboard-300plus for SO<sub>2</sub>, Hubei Cubic-Ruiyi Instrument Co., Ltd. And QGS-08 for CO<sub>2</sub>, Maihak). The oxygen tolerance of the catalyst was measured with feeding 1, 5, and 10 vol% O<sub>2</sub> in the 8000 ppm NO/Ar flow with a total flow rate 30 mL/min. The 5 vol% H<sub>2</sub>O was introduced into the gas mixture by passing the gas stream through a gas saturator at 35 °C to study the effect of H<sub>2</sub>O.

The activity is evaluated with NTN2 according to equation (1),

$$\text{NO Conversion to N}_2 = \frac{2[\text{N}_2]_{\text{out}}}{[\text{NO}]_{\text{in}}} \times 100\% \quad (1)$$

where  $[\text{NO}]_{\text{in}}$  and  $[\text{N}_2]_{\text{out}}$  are the inlet and outlet concentrations of NO and N<sub>2</sub>, respectively.

The reaction rate (r) of NTN2 at 800 °C is calculated with equation (2),

$$r = \frac{F \cdot c \cdot X}{W_{\text{cat}}} \quad (2)$$

where F is the total feed flow (mol/s), c is NO inlet concentration (%), X is NTN2 (%),  $W_{\text{cat}}$  is the weight of catalyst (g).

### 3. Results

#### 3.1. Catalytic activity

The NO direct decomposition activity of the catalyst samples at 500–850 °C is depicted in Fig. 1a. Pure CeO<sub>2</sub>-R exhibits almost negligible activity, achieving only 7.5 % at 850 °C. Similarly, pure BaCoO<sub>3</sub> displays poor activity, with the highest NTN2 at 750 °C being only 12.46 %. However, the activity sharply increased after loading BaCoO<sub>3</sub> on CeO<sub>2</sub> with different morphologies, particularly on the spherical and rod-like CeO<sub>2</sub> samples. The NTN2 at 800 °C follows a distinct order of BCR (78.8 %) > BCS (75.9 %) > BCP (56.9 %) > BaCoO<sub>3</sub> (8.6 %). The activity of BCS and BCR is about 19–22 % higher than that of the BCP sample,

indicating the beneficial interaction between BaCoO<sub>3</sub> and CeO<sub>2</sub> with regular morphologies. The activity of BCR outperforms similar catalysts reported in the literature, as indicated in Table S1. The O<sub>2</sub> yield over BCR is also obtained, and it attains a value of 72.9 % at 800 °C. The amount of O<sub>2</sub> formation is always slightly less than that of N<sub>2</sub> at the same temperature. But if considering the formation of a small amount of NO<sub>2</sub>, the quantities of N<sub>2</sub> and O<sub>2</sub> are nearly balanced for NO direct decomposition, which is also verified in the reference [25,26]. Hence, it seems likely that no accumulation of oxygen is anticipated on the catalyst surface. Subsequently, the NTN2 value is mainly discussed in the NO direct decomposition reaction. The intrinsic rates of the three catalysts at 800 °C are calculated and plotted in Fig. 1b. BCR exhibits the highest rate ( $2.81 \times 10^{-7} \text{ mol g}_{\text{cat}}^{-1} \text{ s}^{-1}$ ) among the three samples.

The O<sub>2</sub> resistance experiment results of BCR are presented in Fig. 1(c). The NTN2 declines from 78.77 % to 74.56 %, 60 % and 50 % at 800 °C under 1, 5 and 10 vol% O<sub>2</sub>, respectively. Furthermore, the BCR sample shows a stable performance in the presence of 5 vol% O<sub>2</sub> over 12 h with only about 5 % decrease in conversion, see Fig. 1(d). The period drops and variation of the activity for the 8000 ppm NO/Ar + 5 vol% O<sub>2</sub> of Fig. 1d may be attributed to the slight change of vacuum degree in the mass spectrometer. Then under the coexistence of 5 vol% O<sub>2</sub> and 5 vol% H<sub>2</sub>O, the NTN2 is stably sustained about 43 % over 12 h after slight decreases from 52 % to 44 % within the initial 5 h. Further, the BCR catalyst experiences an evident activity reduction from 53.1 % to 37.4 % after feeding 1 vol% NO/Ar+5 vol% H<sub>2</sub>O+100 ppm SO<sub>2</sub> for 10.5 h. The NTN2 of BCR catalyst decreases from 50.9 % to 40 % for 11 h under the 1 vol% NO/Ar+5 vol% CO<sub>2</sub> atmosphere. The negative effect of CO<sub>2</sub> is due to the CO<sub>2</sub> can strongly adsorb on the Ba sites of BCR to form carbonate, in agreement with the results in the reference [27]. Therefore, the existence of O<sub>2</sub>, CO<sub>2</sub>, H<sub>2</sub>O and SO<sub>2</sub> in actual flue gas all impede the catalytic performance of BCR catalyst for NO direct decomposition.

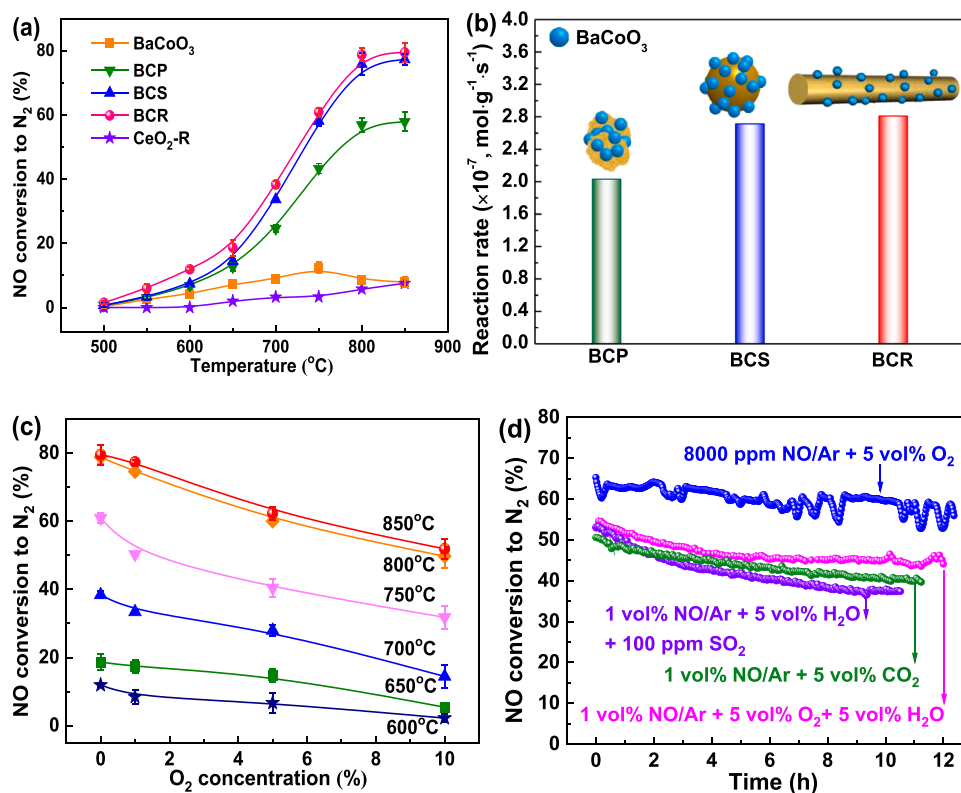


Fig. 1. (a) NO direct decomposition activity over BaCoO<sub>3</sub>, BCP, BCS, and BCR catalysts. (b) Reaction rate of the three catalysts at 800 °C. (c) Activity of BCR with 8000 ppm NO/Ar + 1–10 vol% O<sub>2</sub>. (d) Long-term stability at 800 °C over BCR.

### 3.2. Structure and texture

The XRD patterns of the catalyst samples are presented in Fig. 2. For the BaCoO<sub>3</sub>/CeO<sub>2</sub> samples, only the peaks of CeO<sub>2</sub> phase appear and no diffraction peaks of BaCoO<sub>3</sub> phase are observable no matter of the CeO<sub>2</sub> morphology, indicating well dispersion of BaCoO<sub>3</sub> on CeO<sub>2</sub>. Compared to the patterns of the pure CeO<sub>2</sub> samples, i.e., the p, s and r, see Fig. S3, no shift of CeO<sub>2</sub> peaks are observed. This result suggests that interdiffusion may not occur between the BaCoO<sub>3</sub> and CeO<sub>2</sub> components. The BaCoO<sub>3</sub> sample prepared under the same condition shows an XRD pattern typically for the perovskite phase (JCPDS 70-0363). The Raman spectrum is further performed in Fig. 2(c). For the catalysts containing cerium, the peak at 458–468 cm<sup>-1</sup> belongs to the F<sub>2g</sub> symmetric vibration of oxygen atoms with the fluorite-type structure cerium in CeO<sub>2</sub> [28,29]. Compared with pure CeO<sub>2</sub>-r (468 cm<sup>-1</sup>), the F<sub>2g</sub> peaks of BCP, BCS and BCR are slightly shifted to lower wave number (458 cm<sup>-1</sup>) and peaks intensity becomes weaker, attributing to the addition of BaCoO<sub>3</sub> causing distortion of CeO<sub>2</sub> lattice structure to form more oxygen vacancies, particularly for BCR. There are three additional bands at 232, 598 and 1172 cm<sup>-1</sup>, owing to modes of second-order transverse acoustic (2TA), defect-induced (D), and longitudinal optical (2LO), respectively [27]. The peak at 616 cm<sup>-1</sup> is assigned to the typical vibration peak for perovskite-type structure of BaCoO<sub>3</sub>. The oxygen vacancy (O<sub>v</sub>) concentration (I<sub>598</sub>/I<sub>458</sub>) was also obtained by semiquantitative analysis in Fig. 2(d). It is clearly seen that the O<sub>v</sub> concentration decreases with the sequence of BCR (0.13) > BCS (0.10) > BCP (0.06) > CeO<sub>2</sub>-r (0.02). The highest O<sub>v</sub> concentration in BCR is resulted from the stronger interface interaction between BaCoO<sub>3</sub> and CeO<sub>2</sub>-r, which generates more lattice defects and oxygen vacancy.

The N<sub>2</sub> adsorption-desorption isotherms and pore size distribution curves of the samples are plotted in Fig. 3. All the samples exhibit type IV isotherms with a H3-type hysteresis loop, illustrating that mesopores with good pore connectivity are dominant in Fig. 3a. The SSA of the

samples follows an order of BCR (31.3 m<sup>2</sup>/g) > BCS (28.6 m<sup>2</sup>/g) > BCP (15.6 m<sup>2</sup>/g) > BaCoO<sub>3</sub> (1.2 m<sup>2</sup>/g), which is in consistency with the activity order. It indicates that BCR displays the highest SSA, attributed to the rod morphology of CeO<sub>2</sub> impedes effectively the catalyst sintering and is beneficial to promote the dispersion of active sites [28,29]. The average pore size of BCR is the smallest (15.98 nm) and the pore size distributes in the range of 2–20 nm in Fig. 3b.

Fig. 4 and S4 give the micrographs of the three catalyst samples. The particles in BCP are small agglomerates, while BCS and BCR display well-defined CeO<sub>2</sub> spheres and rods with large particle sizes, Fig. 4a1-c1. The average particle sizes for the BCP, BCS and BCR samples are ~27 nm, ~184 nm and ~5 μm, respectively. The HRTEM images, Fig. 4a2-c2, show that the (110), (102), (101), (211) planes of BaCoO<sub>3</sub> in the samples are observed, corresponding to the lattice fringes of 0.28, 0.21, 0.34 and 0.17 nm, respectively. The CeO<sub>2</sub> supports show *d*-spacing of 0.32 nm with (111) facets for BCP, 0.19 nm with (220) facets for BCS, and 0.19 and 0.32 nm with (220) and (111) facets for BCR. Herein, the major exposed facets are (111) for BCP, (220) for BCS and BCR, in good agreement with the literature [28,29]. Compared with (111) plane of CeO<sub>2</sub> for BCP, the (220) plane of CeO<sub>2</sub> is unstable and has lower formation energy of oxygen vacancy for BCS and BCR. Ba, Co, and Ce elements distribute evenly on all the catalyst samples surface, evidenced by the STEM-EDX mapping graphs in Fig. 4a3, b3 and c3.

### 3.3. Surface states and chemisorption

Fig. 5 plots the XPS Co 2p, Ce 3d and O1s spectra of the three catalyst samples in comparison with those of BaCoO<sub>3</sub> and CeO<sub>2</sub>. The results of elemental analysis calculated with peak area integration are listed in Table 1. The Co 2p spectrum of pristine BaCoO<sub>3</sub> is deconvoluted to distinguish the Co<sup>3+</sup> and Co<sup>2+</sup> contributions. The peaks at 779.6 and 794.8 eV are attributed to Co<sup>3+</sup> while 781.2 and 796 eV are assigned to Co<sup>2+</sup> in Fig. 5a [30]. The peak position of Co<sup>3+</sup> shifts to higher binding

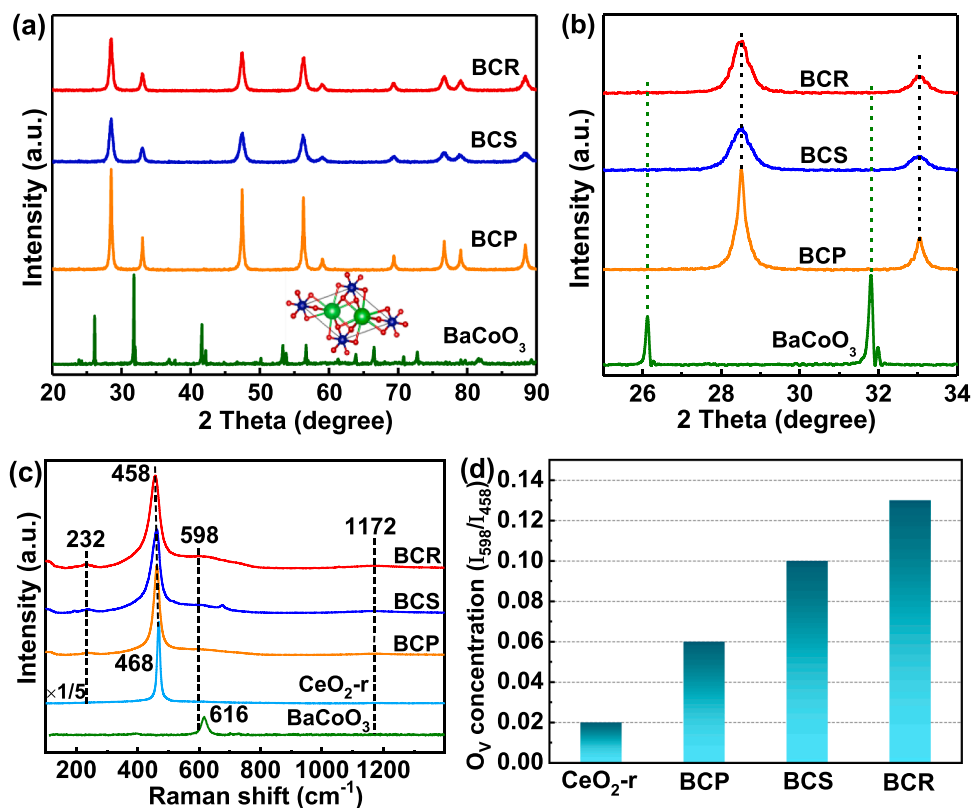


Fig. 2. (a) XRD profiles of BaCoO<sub>3</sub>, BCP, BCS, and BCR catalysts, (b) Enlargement of the XRD profiles with the 2θ range at 25–34°, (c) Raman spectra, and (d) O<sub>v</sub> concentration of catalysts.

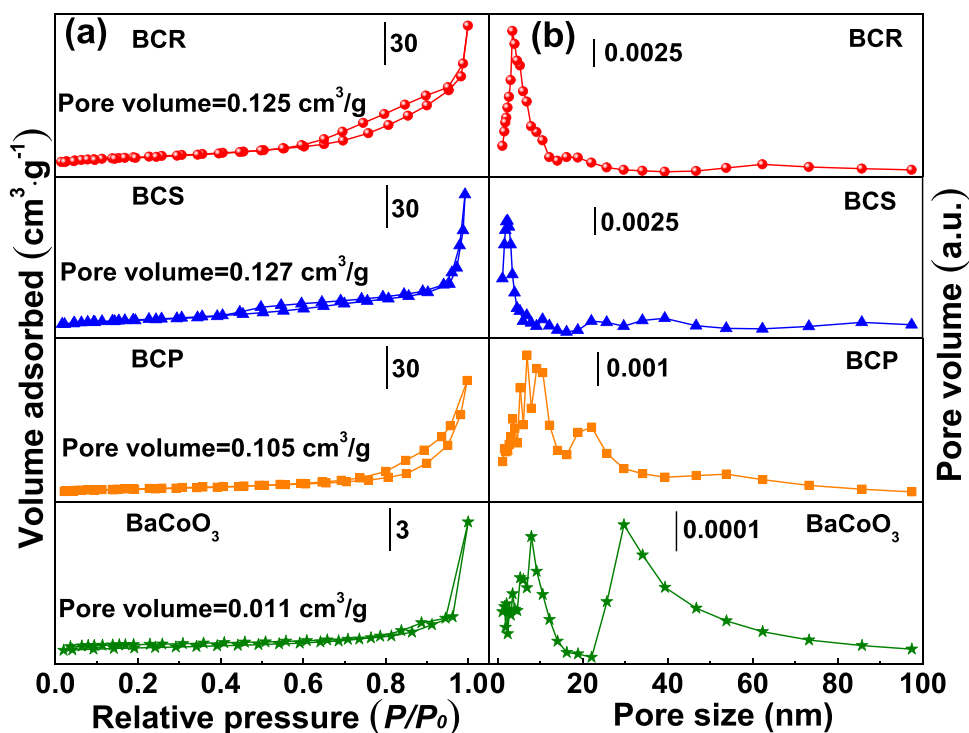


Fig. 3. (a)  $N_2$  adsorption and desorption isotherms, and (b) pore size distributions of the  $BaCoO_3$ , BCP, BCS, and BCR catalysts.

energy ( $\sim 780.5$  eV) in the three catalyst samples. Meanwhile, the part of  $Co^{3+}$  transfers to  $Co^{2+}$  at 796.1 eV owing to the electron transfers of Co species on the surface of  $CeO_2$  support during high temperature calcination step [31]. The semi-quantified  $Co^{3+}/Co^{2+}$  ratio of BCP, BCS, and BCR samples are 2.66, 3.32, and 3.58, respectively. For the Ce 3d spectra in Fig. 5b, the spectra of the three catalyst samples can be fitted to eight peaks (u, u', u'', u''', v, v', v'' and v'''), which are assigned to u' and v' for  $Ce^{3+}$  that favors oxygen vacancies formation, as well as u, u'', v, v'' and v''' for  $Ce^{4+}$  [32]. The amount of  $Ce^{3+}$  is related to the amount of oxygen vacancies ( $O_v$ ) in  $CeO_2$ . The  $Ce^{3+}/Ce^{4+}$  ratio is calculated based on the peak areas, which decreases in the sequence of BCR (0.19) > BCS (0.18) > BCP (0.16), suggesting that relatively higher amount of  $Ce^{3+}$  and  $O_v$  exist in BCR sample. Among the three catalyst samples, the higher ratios of  $Co^{3+}/Co^{2+}$  and  $Ce^{3+}/Ce^{4+}$  in BCR induce electron transfer at the interface between  $BaCoO_3$  and  $CeO_2$ . As shown in Fig. 5 (c), the O 1s spectrum has three peaks at  $\sim 529.2$ ,  $\sim 531.2$  and  $\sim 533.7$  eV, corresponding to lattice oxygen ( $O_{lat}$ ), adsorbed oxygen ( $O_{ads}$ ) and hydroxyl oxygen ( $O_{OH}$ ) species, respectively [33]. The  $O_{ads}/(O_{ads}+O_{lat}+O_{OH})$  ratio has an order of BCR (0.32) > BCS (0.30) > BCP (0.29), in agreement with the ranking of  $Ce^{3+}/Ce^{4+}$  ratio in the catalysts and Raman results (Fig. 2d). The ratio of adsorbed oxygen is correlated to the oxygen vacancy concentration [34]. Thus, the BCR shows a superior activation, transformation and desorption of oxygen via the function of  $Ce^{3+}-[O_v]$ . Furthermore, the characteristic peaks of  $O_{lat}$  for BCP, BCS and BCR are located at lower binding energy at 530.6–530.8 eV than that for pure  $CeO_2-r$  (531.2 eV) and  $BaCoO_3$  (531.15). This observation indicates the higher mobility of lattice oxygen and formation of more oxide ion vacancies by introducing  $CeO_2$  supports in BCP, BCS and BCR catalysts, particularly in BCR, which promotes the catalytic activity.

The pure  $BaCoO_3$  shows three peaks in its  $H_2$ -TPR profile Fig. 6(a), labeled as  $\alpha_1$  (362 °C),  $\alpha_2$  (499 °C) and  $\alpha_3$  (610 °C), corresponding to the reduction steps of  $Co^{4+}$  to  $Co^{3+}$ ,  $Co^{3+}$  to  $Co^{2+}$  and maybe  $Co^{2+}$  to  $Co^0$ , respectively [35,36]. For pure  $CeO_2-r$ , two peaks at  $\beta_1$  (595 °C) and  $\beta_2$  (821 °C) are assigned to the reduction of surface and bulk  $Ce^{4+}$  to  $Ce^{3+}$ , respectively [37]. It is explicit that the  $\alpha$  peak (including  $\alpha_1$  at 294 °C,  $\alpha_2$  at 340 °C and  $\alpha_3$  at 360 °C) for BCP, BCS and BCR catalysts shift to lower

temperatures and still mainly exist as  $Co^{3+}$  compared to those of the pure  $BaCoO_3$ . Meanwhile the  $\beta_1$  reduction peak almost disappears in all three catalysts. Obviously, the  $BaCoO_3$  component is highly dispersed on the  $CeO_2$  surface and strong synergy between two phases, benefiting to promote the reduction activity. In addition, the actual  $H_2$  consumption of  $\alpha$  peak (Fig. 6d) follows order BCR (254.7  $\mu mol/g$ ) > BCS (217.3  $\mu mol/g$ ) > BCP (186.5  $\mu mol/g$ ). The  $H_2$  consumption of Cerium species ( $\beta$  peak in Fig. 6d) is similar in these three catalysts. These mean that the more  $Co^{3+}$  species reduction and stronger interaction occurs in BCR, contributing to enhanced catalytic activity.

The mobility of lattice oxygen is examined by  $O_2$ -TPD in Fig. 6(b). Two peaks contain adsorbed oxygen on the oxide ion vacancies ( $\sim 730$  °C) and lattice oxygen ( $\sim 860$  °C) in the catalysts [38]. Compared with the desorption peak temperature of lattice oxygen in pure  $BaCoO_3$ , the peaks of BCP, BCS and BCR shift to lower temperatures orderly, suggesting that different morphology of  $CeO_2$  effectively weakens the Co-O bond strength and promotes the desorption of oxygen from  $BaCoO_3$ . Particularly, the BCR owns the highest lattice oxygen mobility, which is conducive to enhance activity and resistance of  $O_2$ .

Fig. 6(c) displays the NO-TPD profiles to analysis NO sorption of catalysts. There are two NO desorption peaks at 314 and 507 °C for pure  $BaCoO_3$ , meanwhile NO desorbs at 256 and 525 °C for pure  $CeO_2-r$  [39, 40], which are attributed to weak and strong NO adsorption species on different components, respectively. The BCP, BCS and BCR show similar NO desorption profiles but all bigger than that of pure samples due to the interaction effect may produce more electron coordination environment on the active sites to adsorb NO. Combined to the calculated NO desorption amount of catalysts (Fig. 6d), decreasing in the order of BCR (318.3  $\mu mol/g$ ) > BCS (260.3  $\mu mol/g$ ) > BCP (228.1  $\mu mol/g$ ) >  $BaCoO_3$  (122.3  $\mu mol/g$ ) >  $CeO_2-r$  (75.8  $\mu mol/g$ ). BCR exhibits the highest NO adsorption capacity and hence increase activity. Accordingly, the reducibility, mobility of lattice oxygen and NO sorption of catalysts decrease in the sequence of BCR > BCS > BCP >  $BaCoO_3$ , in agreement with the variation of activity results (Fig. 1a).

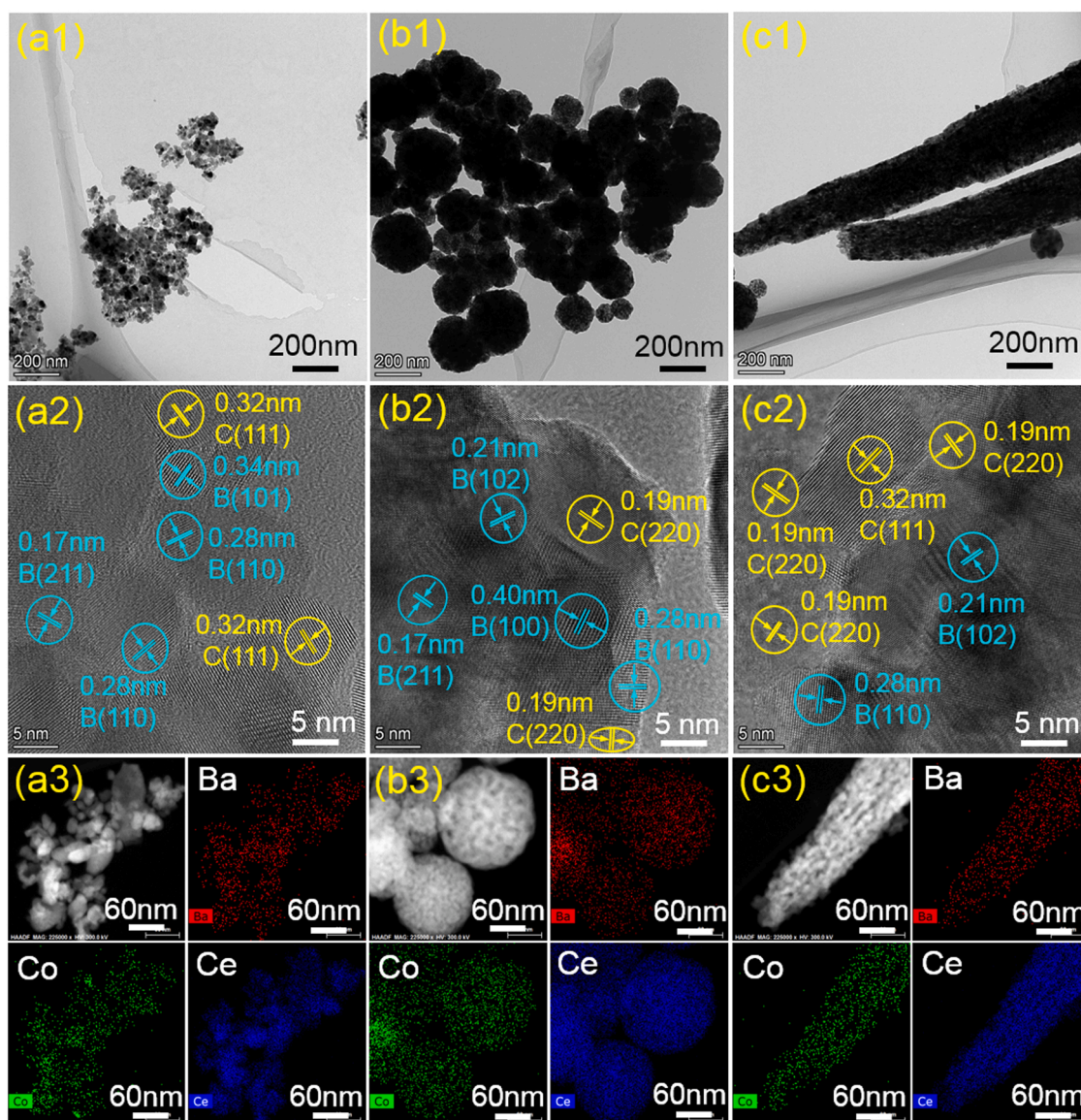


Fig. 4. TEM, HRTEM and STEM-EDX mapping for different catalysts: (a1, a2, a3) BCP, (b1, b2, b3) BCS, and (c1, c2, c3) BCR. B represents BaCoO<sub>3</sub>, and C stands for different CeO<sub>2</sub> supports.

### 3.4. *In situ* DRIFT and isotopic (<sup>18</sup>O<sub>2</sub>) tracing experiments

To further investigate the adsorbed intermediates and reaction behavior of the samples, *in-situ* DRIFT is applied with BCR sample (Fig. 7), and corresponding detailed assignment of NO adsorption bands are listed in Table 2. As shown in Fig. 7(a), the *in-situ* DRIFT profiles are recorded under 1 vol% NO/He from 30 to 600 °C. The intensity bands for nitrous oxide (N<sub>2</sub>O) at 2240 and 2210 cm<sup>-1</sup> are weak at 30 °C and then gradually disappear with the temperature increase from 200 to 600 °C (Fig. 7b) [41]. In general, the N<sub>2</sub>O acts as main intermediate and decomposes quickly at higher temperature and few parts of N<sub>2</sub>O still adsorb on the catalyst surface [41]. The adsorbed mononitrosyl (NO<sup>\*</sup>) at 1930 and 1845 cm<sup>-1</sup> are assigned to Co<sup>3+</sup> sites, revealing that the cobalt species acts as the main active center for NO decomposition reaction [20,42,43]. The intensity of mononitrosyl peak becomes weaker with the temperature increase, whilst the monodentate nitrite (NO<sub>2</sub><sup>-</sup>) adsorbed on Co<sup>3+</sup> (1520 cm<sup>-1</sup>) becomes stronger, suggesting that the subsequent transformation from NO<sup>\*</sup> to NO<sub>2</sub><sup>-</sup> on the Co species of catalyst [44]. The band at 1774 cm<sup>-1</sup> for asymmetric nitric oxide dimer ((-NO)<sub>2</sub>/-NOON) is formed on Co<sup>2+</sup> during the NO adsorption process

[20,21,45], in agreement with the IM2 structure in the following DFT results of Fig. 9(c) and (d). The intense bands of NO<sup>\*</sup> on Co<sup>3+</sup> and weak (-NO)<sub>2</sub> species formed on Co<sup>2+</sup> show the Co<sup>3+</sup>/Co<sup>2+</sup> cycles supply effective electrons for the NO adsorption and transformation, in consistency with the ratio of Co<sup>3+</sup>/Co<sup>2+</sup> in XPS results (Fig. 5a). In addition, the chelating bidentate nitrite (NO<sub>2</sub><sup>-</sup>) adsorbed on CeO<sub>2</sub> (1238 and 813 cm<sup>-1</sup>) turns weaker, probably due to NO<sub>2</sub><sup>-</sup> desorbs in the form of NO<sub>2</sub> molecule at the certain temperature [46]. The strong bands at 1608–1013 cm<sup>-1</sup> are attributed to the nitrate species with different adsorption states [26,47]. Those adsorption species become more stable and stronger with the temperature increase to 200 °C, particularly nitrate free ion to 400 °C, and then decompose at the higher temperature with the decreased band intensity until almost disappear at 600 °C. The contribution of Ba is more likely to promote the reduction of Co ions and formation of oxygen vacancy for stable ABO<sub>3</sub> perovskite type catalyst [24].

The effect of O<sub>2</sub> on the adsorbed intermediate species over the BCR was also explored under 1 vol% NO+2 vol% O<sub>2</sub>/He in Fig. 7(c) and (d). The intensity of bridging bidentate nitrate (1608 cm<sup>-1</sup>) and monodentate nitrate (1408 cm<sup>-1</sup>) become stronger than that of 1 vol% NO/

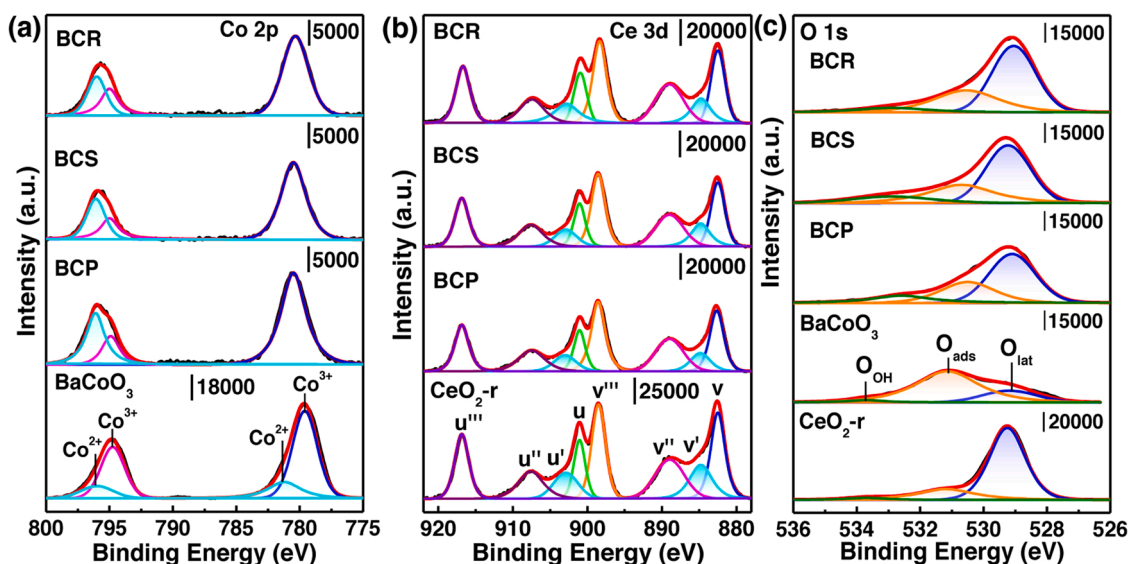


Fig. 5. XPS spectra of catalysts (a) Co 2p (b) Ce 3d, and (c) O 1 s for BaCoO<sub>3</sub>, CeO<sub>2</sub>-r, BCP, BCS, and BCR catalysts.

**Table 1**  
Surface atomic ratios of catalysts obtained by XPS semi-quantitative analysis.

Catalysts	Surface area ratio		
	Co <sup>3+</sup> /Co <sup>2+</sup>	Ce <sup>3+</sup> /Ce <sup>4+</sup>	O <sub>ads</sub> /(O <sub>ads</sub> +O <sub>lat</sub> +O <sub>OH</sub> )
CeO <sub>2</sub> -r	–	0.23	0.21
BaCoO <sub>3</sub>	2.69	–	0.75
BCP	2.66	0.16	0.29
BCS	3.32	0.18	0.30
BCR	3.58	0.19	0.32

He condition, and even maintain at 600 °C although the similar variation occurs for other peaks. It infers that the O<sub>2</sub> facilitates the formation of stable nitrate species on the surface, restraining the activity of catalyst in some extent [48]. Notably, the intensity of adsorbed NO on Co species, N<sub>2</sub>O and nitrite species is similar under both conditions, which evidences that the Co species acts as main active center, and the active intermediate species are N<sub>2</sub>O and nitrite species instead of nitrate species. The addition of CeO<sub>2</sub> support effectively protects Co species from O<sub>2</sub> atmosphere.

The isotopically labeled <sup>18</sup>O<sub>2</sub> gas as reactant in steady-state is used to further distinguish the intrinsic effect with/without O<sub>2</sub> for NO direct decomposition, as shown in Fig. 8. Firstly, the blank calibration without catalyst at room temperature was performed in the reactor to clarify the actual components of reactant gases (Fig. 8a). The standard transient response curves of NO and <sup>18</sup>O<sub>2</sub> were detected after introducing the mixed gases (1 vol% NO + 1 vol% <sup>18</sup>O<sub>2</sub>/Ar). Both NO and <sup>18</sup>O<sub>2</sub> signals increase sharply and simultaneously at the beginning of mixed gases feeding to the reactor, which quickly produces response signals of gases. Then NO and <sup>18</sup>O<sub>2</sub> curves keep stable and other gas signals (N<sub>2</sub>, <sup>16</sup>O<sub>2</sub> and <sup>16</sup>O<sup>18</sup>O) were not monitored, indicating that no other impurity gas existed in the mixed reactant gases. The pure Ar (30 mL/min) was purged to remove reactants existed in the reactor after realizing steady state of each reaction stage. The effect of O<sub>2</sub> on the NO direct decomposition was illustrated in Fig. 8(b). Before the reaction, the fresh BCR was pretreated and kept in Ar (30 mL/min) at 800 °C. The evident and stable signals of N<sub>2</sub> and <sup>16</sup>O<sub>2</sub> can be observed owing to the NO efficient decomposition at 800 °C over the BCR catalyst after switching 1 vol% NO/Ar, while no by-product forms (Fig. S5). Then the mixed gas of 1 vol% NO + 1 vol% <sup>18</sup>O<sub>2</sub>/Ar was fed to the reactor after purging with pure Ar. It is noted that the three different O<sub>2</sub> isotopomer products (<sup>16</sup>O<sub>2</sub>, <sup>16</sup>O<sup>18</sup>O and <sup>18</sup>O<sub>2</sub>) were detected in turn. Firstly, large amounts of <sup>16</sup>O<sub>2</sub>

produced quickly, which decreased rapidly and then increased gradually to steady value with increasing reaction time, attributed to NO decomposition product and releasing from the BCR itself. The heteroexchange of <sup>18</sup>O<sub>2</sub> with original <sup>16</sup>O in catalyst was noticed at high temperature with high oxygen mobility [49]. After <sup>16</sup>O<sub>2</sub> desorption from catalyst, the oxygen vacancy sites generated accordingly are simultaneously replenished by the surface adsorption and dissociation of gaseous <sup>18</sup>O<sub>2</sub> molecules followed by the lattice oxygen diffusion, resulting in the <sup>16</sup>O<sub>2</sub> signal produced quickly and then decreased [50]. The N<sup>18</sup>O should be considered to produce because of the same *m/z* (32) to <sup>16</sup>O<sub>2</sub>. The signal of N<sup>18</sup>O/<sup>16</sup>O<sub>2</sub> increased gradually to steady with increasing time reflects that the oxygen of NO can be exchanged with the part of adsorbed <sup>18</sup>O from the catalyst surface to form N<sup>18</sup>O, which is also supported by Damma et al. [51]. Subsequently, the cross-labeled <sup>16</sup>O<sup>18</sup>O generated quickly, corresponding to the rapid decrease of <sup>16</sup>O<sub>2</sub>, suggesting that the suitable lattice <sup>18</sup>O species adsorbed on the surface oxygen vacancies start to participate NO decomposition and promote <sup>16</sup>O<sup>18</sup>O and N<sub>2</sub> formation, in associate with the stable N<sub>2</sub> signal at that time. Afterwards, the <sup>18</sup>O<sub>2</sub> increased gradually and tend to reach steady state with the increase of reaction time, attributed to excess gaseous <sup>18</sup>O<sub>2</sub> fills more oxygen vacancies firstly but can not exchange completely, resulting in a competitive adsorption with NO on the oxygen vacancies and the catalytic activity decreases slightly, corresponding to a gradual decrease of N<sub>2</sub> formation after about 60 min. It suggests that the updated and appropriate lattice oxygen (<sup>18</sup>O) species accelerate the reaction at the beginning of O<sub>2</sub> addition. However, excess <sup>18</sup>O<sub>2</sub> produces an inhibition effect of NO adsorption and transformation. In addition, very small amounts of intermediate species (N<sub>2</sub><sup>18</sup>O, N<sup>16</sup>O<sup>18</sup>O and N<sup>16</sup>O<sub>2</sub>) can be obtained, which may not decompose (Fig. S4). On the basis of isotopic (<sup>18</sup>O<sub>2</sub>) tracing studies, it can be found that moderate labile oxygen species on the surface oxygen vacancies of catalyst play a key role in NO direct decomposition reaction.

### 3.5. DFT calculation results

To deeply understand the synergy effect between BaCoO<sub>3</sub> and CeO<sub>2</sub> support of catalyst and direct decomposition mechanism of NO, the DFT+U method is performed to study this reaction. The reaction pathway is connected by initial state (IS), intermediate (IM), transition state (TS) and final state (FS). Based on catalyst morphology of TEM and XRD, pure BaCO<sub>3</sub>(101), BaCO<sub>3</sub>/CeO<sub>2</sub> (110) for BCS and BCR, and BaCO<sub>3</sub>/CeO<sub>2</sub> (111) for BCP models are constructed in Fig. 9(a). The reaction mechanisms of NO on BaCoO<sub>3</sub>/CeO<sub>2</sub> (110) and BaCoO<sub>3</sub>/CeO<sub>2</sub>

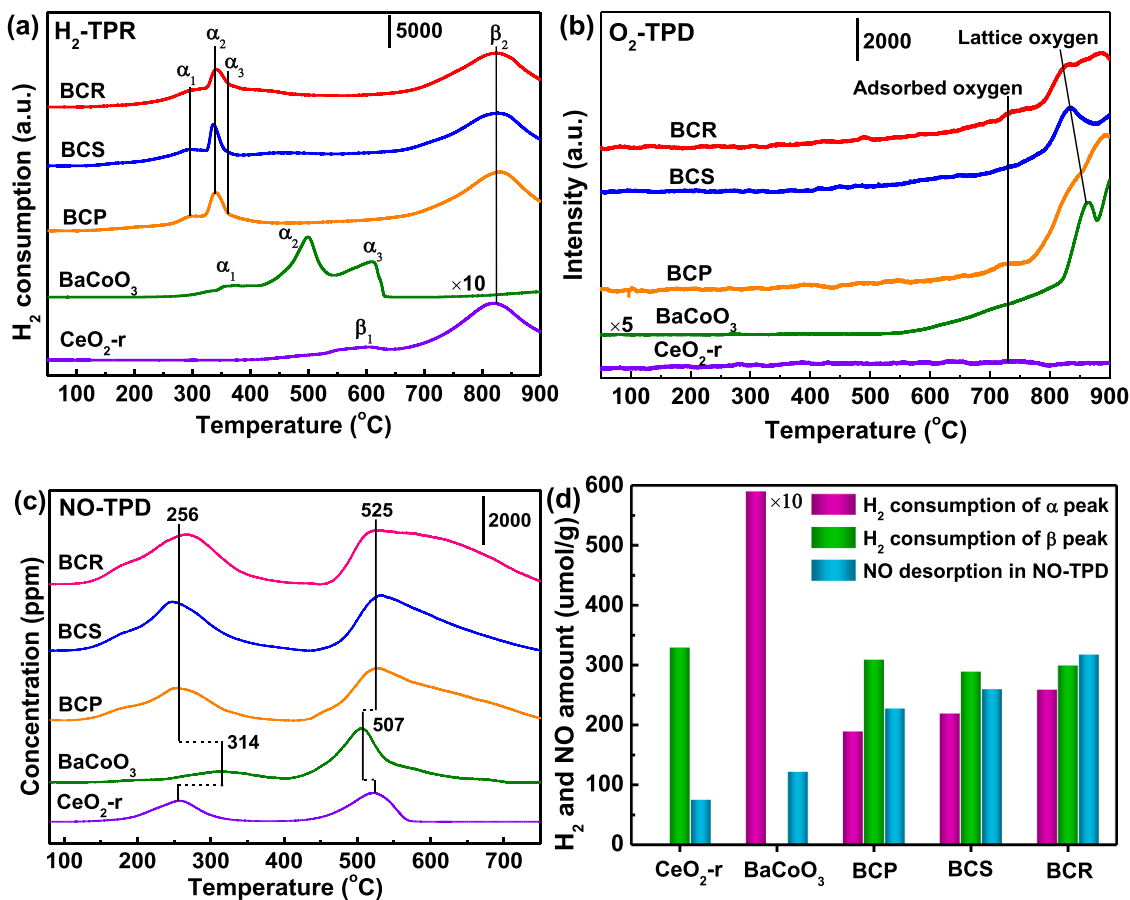


Fig. 6. (a) H<sub>2</sub>-TPR, (b) O<sub>2</sub>-TPD, (c) NO-TPD and (d) H<sub>2</sub> consumption and NO adsorption for catalysts.

(111) surfaces have been explored, as in Fig. 9. The adsorption of NO on the two different surfaces has been investigated. NO can be adsorbed on the surfaces through either the N-end or the O-end. Adsorption structures through the N-end are more stable on both BaCoO<sub>3</sub>/CeO<sub>2</sub> (110) and BaCoO<sub>3</sub>/CeO<sub>2</sub> (111) surfaces, with adsorption energies of 0.82 eV and 0.57 eV, respectively. Namely, NO adsorption on BaCoO<sub>3</sub>/CeO<sub>2</sub> (110) releases ~0.25 eV more energy compared to on BaCoO<sub>3</sub>/CeO<sub>2</sub> (111). On the other hand, adsorption through the O-end on the surfaces has lower energies, with values of 0.38 eV and 0.20 eV, respectively. The direct decomposition mechanism of NO on the BaCoO<sub>3</sub> (101) surface is also proposed in Fig. S5. Similarly, NO is also adsorbed through the N-end on the surface with the bigger adsorption energy (0.46 eV) than the O-end on the surface (0.33 eV), suggesting that the structure with NO adsorbed through the N on the surface is more advantageous on BaCoO<sub>3</sub>. As the second NO molecule is adsorbed on the surface, the two NO molecules can directly react to form a bridging \*NOON species (IM2). This reaction process releases energies of 1.72 eV for BaCoO<sub>3</sub>/CeO<sub>2</sub> (110) and 1.99 eV for BaCoO<sub>3</sub>/CeO<sub>2</sub> (111). Unlike on BaCoO<sub>3</sub> (Fig. S6), this transition state can occur spontaneously without the energy barrier on BaCoO<sub>3</sub>/CeO<sub>2</sub>. As the reaction progresses, the \*NOON species undergoes a turnover to adsorb on the surface through the O-end (IM3). Different from that on BaCoO<sub>3</sub> with the negligible energy (0.08 eV), this process requires energies of 0.70 eV (BaCoO<sub>3</sub>/CeO<sub>2</sub> (110)) and 1.01 eV on (BaCoO<sub>3</sub>/CeO<sub>2</sub> (111)). This can be attributed to the stronger interaction between the N-end and the Co adsorption sites. Alternatively, NO can also directly form the IM3 structure through the O-end. After the second NO molecule is adsorbed through the O-end on the surface, it can directly react with the already adsorbed NO to form a \*NOON species connected on the surface through the O-end. This process is also a barrierless reaction. As one of the N-O bonds in \*NOON is broken (TS1), the dissociated \*O atom fills an oxygen vacancy on the

surface, while \*N<sub>2</sub>O molecule adsorbs on the surface through the O-end (IM4), in agreement with *in situ* DRIFT results. The energy barrier for this process is ~0.6 eV. Finally, after overcoming an energy barrier of about 1 eV, the N-O bond in \*N<sub>2</sub>O is broken (TS2). The \*O atom fills the vacancy, while N<sub>2</sub> desorbs from the surface. The reaction energies for this process are 1.11 eV for BaCoO<sub>3</sub>/CeO<sub>2</sub> (110) and 1.26 eV for BaCoO<sub>3</sub>/CeO<sub>2</sub> (111), respectively. In addition, the energy barrier of O<sub>2</sub> adsorbed on the Co site is about 0.36 eV for BaCoO<sub>3</sub>/CeO<sub>2</sub> (110), which is lower than that of NO adsorbed on the Co site, suggesting the NO is easier to adsorb on active sites.

## 4. Discussion

### 4.1. Intrinsic structure-activity relationship

The intrinsic catalytic activity of the BaCoO<sub>3</sub>/CeO<sub>2</sub> catalyst shows a significant morphology-dependent behavior, which is displayed in Scheme 1. The addition of CeO<sub>2</sub> with different morphology induces a sensitive perovskite-support interaction (PSI). BCR owns the largest average particle size (~5 μm) and SSA with regular rod appearance, which provides enough reactive interface area to adsorb and transform reactants, which not only alleviates the sintering of BaCoO<sub>3</sub> effectively but also strengthens the synergy between BaCoO<sub>3</sub> and CeO<sub>2</sub>-r (Figs. 3 and 4). Hence, the well dispersed BaCoO<sub>3</sub> on the surface of CeO<sub>2</sub> support, and both components contact with each other closely to form effective reaction interface is beneficial for strong interaction to promote activity in NO direct decomposition. Compared with (111) plane of CeO<sub>2</sub> for BCP, the (220) plane is unstable and has lower formation energy of oxygen vacancy for BCS and BCR. Meanwhile, the higher ratios of Co<sup>3+</sup>/Co<sup>2+</sup>, Ce<sup>3+</sup>/Ce<sup>4+</sup>, O<sub>ads</sub>/(O<sub>ads</sub>+O<sub>lat</sub>+O<sub>OH</sub>) and O<sub>v</sub> concentration of the BCR sample were induced by PSI, exhibiting more active electron

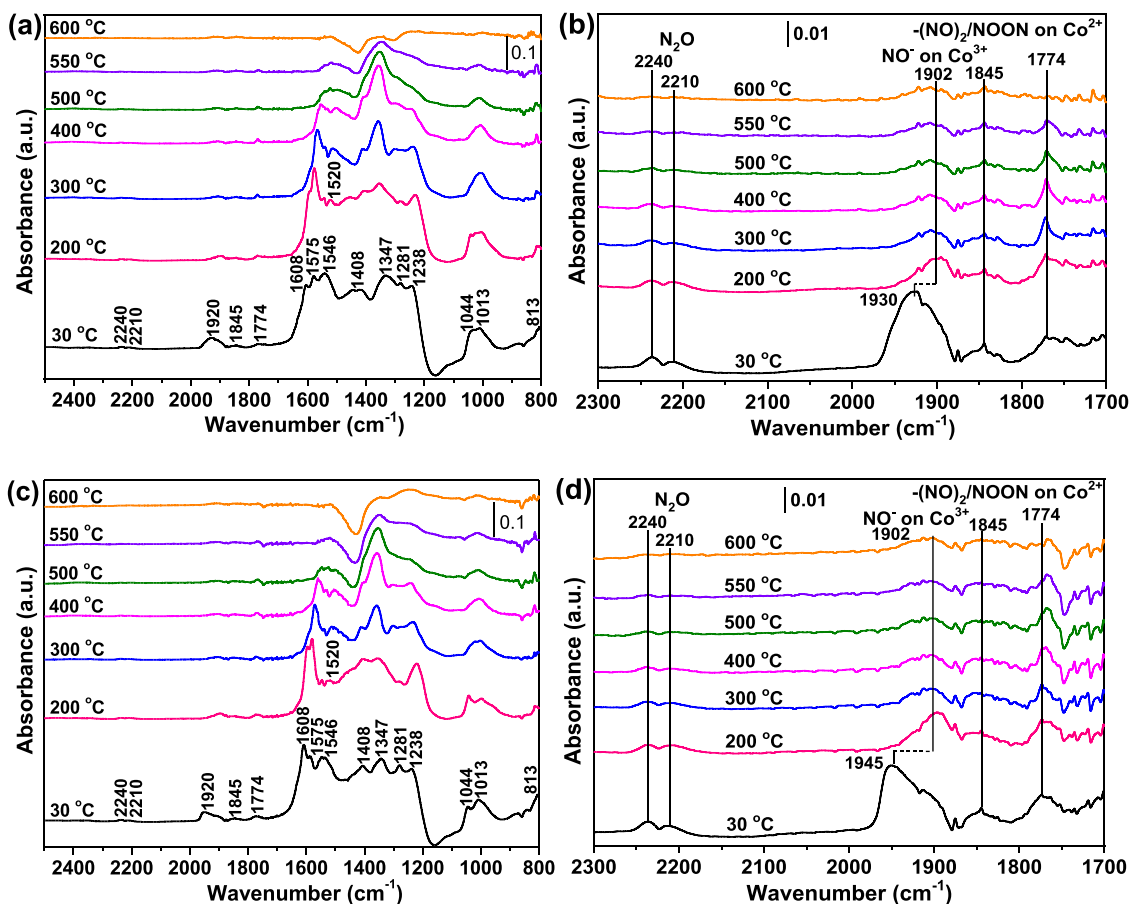


Fig. 7. *In situ* DRIFT profiles of BCR under (a), (b) 1 vol% NO/He, and (c), (d) 1 vol% NO+2 vol% O<sub>2</sub>/He at 30–600 °C.

transfer and oxygen vacancy at the BCR interface (Fig. 5). The BCR surface contains Co<sup>3+</sup> and Co<sup>2+</sup> ions with an electron configuration of  $t_{2g}^4 e_g^2$  and  $t_{2g}^5 e_g^2$ , respectively [52]. The Co<sup>3+</sup> possesses more unpaired electron than Co<sup>2+</sup>, resulting in a promoting affinity for nitrogen donors when the ratio of Co<sup>3+</sup>/Co<sup>2+</sup> increase [52]. By comparing the PSI on BaCoO<sub>3</sub> and BaCoO<sub>3</sub>/CeO<sub>2</sub>, we can observe that BaCoO<sub>3</sub>/CeO<sub>2</sub> exhibits a stronger adsorption ability to NO. Furthermore, the NO adsorption sites on BaCoO<sub>3</sub>/CeO<sub>2</sub> allow for the direct formation of \*NOON species without the energy barrier. This characteristic enhances the catalytic performance of BaCoO<sub>3</sub>/CeO<sub>2</sub>, attributed to the synergistic effects between BaCoO<sub>3</sub> and CeO<sub>2</sub>. The CeO<sub>2</sub> promotes the stabilization of the adsorbed species, leading to stronger NO adsorption. The proximity of the adsorption sites facilitates the direct formation of \*NOON species, which further enhances the catalytic activity of BaCoO<sub>3</sub>/CeO<sub>2</sub>. Another factor contribute to the stronger catalytic performance of BaCoO<sub>3</sub>/CeO<sub>2</sub> (110) is the influence of oxygen vacancy (O-vacancy). The electrons left behind with more oxygen vacancy formation which reduces Ce<sup>4+</sup> (<sup>2</sup>F) to Ce<sup>3+</sup> (<sup>1</sup>S) ions [53]. It is well known in DFT results that the O vacancy tends to be on the CeO<sub>2</sub> (110) surface (1.69 eV). On CeO<sub>2</sub> (111) surfaces, it is usually located at subsurface sites (1.83 eV). It is also consistent with the experimentally observed higher concentration of oxygen vacancies in BCR samples. Consequently, oxygen vacancies located on the surface are more prone to migrate to the BaCoO<sub>3</sub>, enhancing the coordination effects and promoting catalyst activity. Therefore, compared to BaCoO<sub>3</sub>/CeO<sub>2</sub> (111) for BCP, the combination of stronger NO adsorption and the presence of surface oxygen vacancies in BaCoO<sub>3</sub>/CeO<sub>2</sub> (110) for BCS and BCR contribute to its superior catalytic performance, in agreement with the activity results. That highlight the importance of surface orientation and oxygen vacancy distribution in determining the catalytic properties of composite materials.

Electronic interactions always occur at solid-solid interfaces and are simply driven by the principles of the system energy minimization and the continuity of the electric potential in the solid phases [54–56]. The redox interaction effect (Co<sup>3+</sup> + Ce<sup>3+</sup> ↔ Co<sup>2+</sup> + Ce<sup>4+</sup>) produces long-range charge transfer and thereby causes more oxygen vacancies under the stable electric field on the concomitant BCR interface, suggesting the high availability of reaction environment on BCR with rod-like CeO<sub>2</sub>. The BCR active interface is likely formed via a bonding between Co species in BaCoO<sub>3</sub> and the surface defect sites on both perovskite and ceria (Ce<sup>3+</sup>-O<sub>v</sub>) species. The similar results of interface effect between metal site and the morphology of CeO<sub>2</sub> supports for other catalytic reactions were also verified in the literatures [18,57–60]. To sum up, the construction of active interface on BCR improves PSI and activates electronic interactions, promoting reducibility, lattice oxygen mobility with more Oxygen vacancy and NO adsorption and boosting the catalytic performance in NO direct decomposition reaction.

#### 4.2. Proposed reaction pathways

The active sites of Co species and oxygen vacancies on the interfaces in BCR were observed. Combined with *in situ* DRIFT, isotopic (<sup>18</sup>O<sub>2</sub>) exchange and DFT results, the NO molecules are effectively adsorbed on the Co species, but a competitive adsorption between NO and O<sub>2</sub> occurs on the oxygen vacancies after introducing O<sub>2</sub>, resulting in a decrease of catalytic activity with the increasing operation time, in agreement with the results presented in Fig. 1d. Ba is more likely to promote the reduction of Co ions and formation of oxygen vacancy for stable ABO<sub>3</sub> perovskite type catalyst. Therefore, the reaction mechanism of NO direct decomposition over BCR catalyst is proposed in Scheme 2. NO molecule initially adsorbs on the active sites of Co species to form the mononitrosyl (NO\*), and then interacts with an adjacent NO\* on [ ] of active

**Table 2**  
Detailed assignment of NO adsorption bands by *in situ* DRIFT profiles.

Wavenumber (cm <sup>-1</sup> )	Bond	Vibration	Adsorbed species	Structure
2240, 2210	N-N	$\nu$	N <sub>2</sub> O	-
1930, 1902, 1845	-N-O	$\nu_{as}$	NO on Co <sup>3+</sup>	
1774	-O=N	$\nu$	Asymmetric nitric oxide dimer, -(NO) <sub>2</sub> /NOON on Co <sup>2+</sup> sites	
1608, 1044	N=O	$\nu$	Bridging bidentate nitrate, (NO <sub>3</sub> )	
1575, 1546	N=O	$\nu$	Chelating bidentate nitrate, (NO <sub>3</sub> )	
1520	-O-N-O	$\nu$	Monodentate nitrite (NO <sub>2</sub> ) on Co <sup>3+</sup>	
1408	N=O	$\nu$	Monodentate nitrate, (M-NO <sub>3</sub> )	
1347, 1281, 1013	N-O	$\nu_{as}$ $\nu_s$	Nitrate free ion Monodentate nitrate, (M-NO <sub>3</sub> )	
1238, 813	NO <sub>2</sub>	$\nu_{as}$	Chelating bidentate nitrite (NO <sub>2</sub> ) on CeO <sub>2</sub>	

\* $\nu$  represents the stretching vibration;  $\nu_{as}$  represents the asymmetric stretching vibration;  $\nu_s$  represents the symmetric stretching vibration; M represents metal sites.

sites over the active interface to produce NOON\*, as discussed in literature [61]. The easy formation of NOON\* decomposes into N<sub>2</sub>O\* and the dissociated \*O atom fills an oxygen vacancy on the surface to form active oxygen ([O<sup>2-</sup>]) species, verified in the *in-situ* DRIFT and DFT results. The

high mobility of lattice oxygen promotes this process, which is evidenced by the O<sub>2</sub>-TPD and XPS results. The suitable amounts of lattice oxygen and oxygen vacancies on the surface of catalyst is beneficial to both the formation and consumption of NO\*. Then the intermediates of \*N<sub>2</sub>O is broken with reaction energies at 1.11 eV to produce N<sub>2</sub> and the \*O atom fills the vacancy (Fig. 9b). The adjacent active \*O atom to further form O<sub>2</sub>. Therefore, the decomposition of N<sub>2</sub>O\* is likely the rate-determining step (RDS) in NO direct decomposition over BCR. In addition, the original lattice <sup>16</sup>O is consumed and replaced with the formation of lattice <sup>18</sup>O via occupying more [ ] of the catalyst after adding excess gaseous <sup>18</sup>O<sub>2</sub> in the isotopic (<sup>18</sup>O<sub>2</sub>) exchange experiment. Herein the competitive adsorption of NO and O<sub>2</sub> on the [ ] mainly occurs in this step. The formed N<sub>2</sub>O\* species quickly decomposes into N<sub>2</sub> and another adsorbed oxygen (O\*). Finally, the adjacent adsorbed oxygen (O\*) species combine to produce O<sub>2</sub> and release active sites, which is ready for next catalytic cycle. The production of <sup>16</sup>O<sup>18</sup>O is well verified with the formation and reaction of new lattice <sup>18</sup>O in the above-mentioned isotopic (<sup>18</sup>O<sub>2</sub>) tracing results. In this reaction mechanism, not only Co species acted as main active sites, but also oxygen vacancies play an important role on the BCR active interface for NO decomposition. The intrinsic effect with O<sub>2</sub> for NO direct decomposition shows that the suitable amount of lattice oxygen promotes the nitrite species formation at the beginning of the reaction. However, excessive amount of O<sub>2</sub> occupies more oxygen vacancies and inhibits the NO\* formation and transformation of NO\* into N<sub>2</sub>O\* due to the competitive adsorption of NO and O<sub>2</sub> on the oxygen vacancies, impeding the NO direct decomposition. The mobility of lattice oxygen and timely desorption of O<sub>2</sub> over the catalyst are crucial to further improve the catalytic activity and tolerance of O<sub>2</sub>. These results contribute to our understanding of the perovskite-support interaction and reaction mechanisms and energetics involved in the NO adsorption and reaction processes on BaCoO<sub>3</sub>/CeO<sub>2</sub> systems, shedding light on the potential catalytic activity of these materials in NO-related reactions.

## 5. Conclusion

The distinct structure-activity relationships of the BaCoO<sub>3</sub>/CeO<sub>2</sub> catalysts were investigated using CeO<sub>2</sub> with conventional small particle (p), sphere (s) and rod (r) morphologies. The NTN2 at 800 °C decreases in the order of BCR (78.9 %) > BCS (75.9 %) > BCP (56.9 %) > BaCoO<sub>3</sub> (8.6 %). BCR also exhibits a high durability (maintain NO conversion ~60 %) in the presence of 5 vol% O<sub>2</sub> for 12 h. Such superior catalytic activity and O<sub>2</sub> tolerance of BCR are attributed to the strong PSI on the oxide phases interface. The CeO<sub>2</sub> rod enhances the sintering resistance with high surface area, redox activity, mobility of active lattice oxygen and NO adsorption capability. We proposed a reaction mechanism that

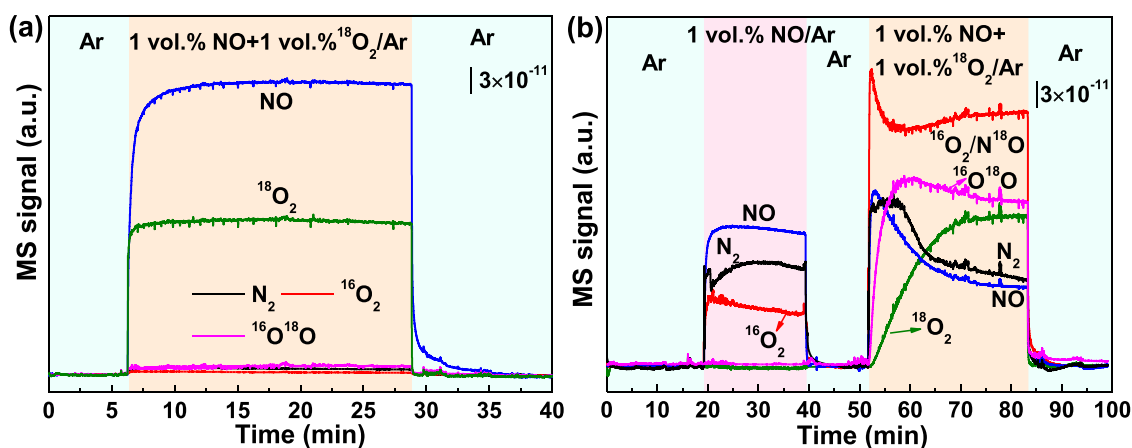


**Fig. 8.** Isotopic (<sup>18</sup>O<sub>2</sub>) exchange experiments (a) blank calibration without catalyst at room temperature, and (b) NO direct decomposition processes at 800 °C over BCR at 1 vol% NO/Ar and 1 vol% NO + 1 vol% <sup>18</sup>O<sub>2</sub>/Ar conditions.

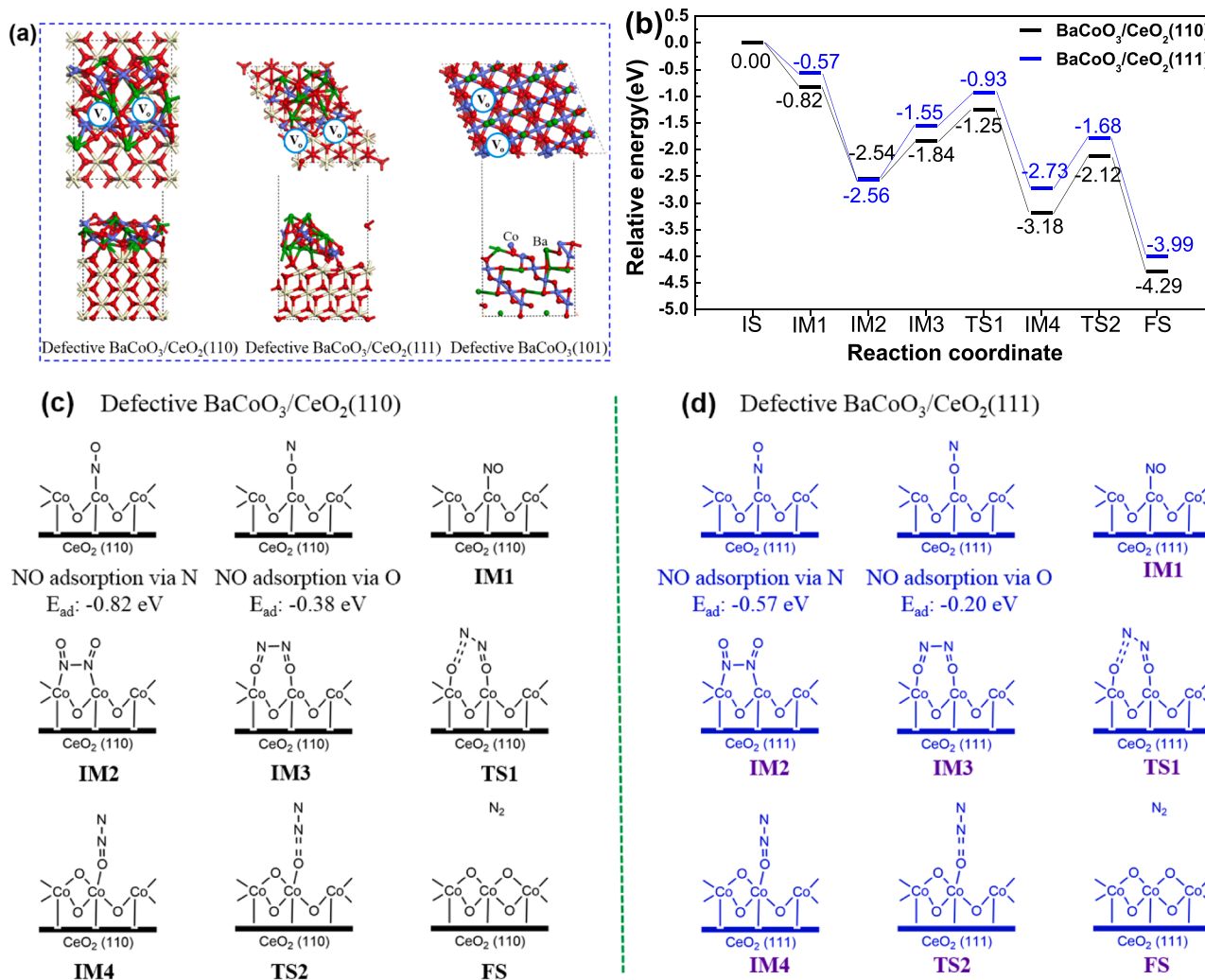
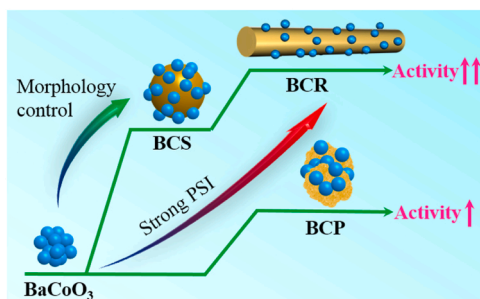
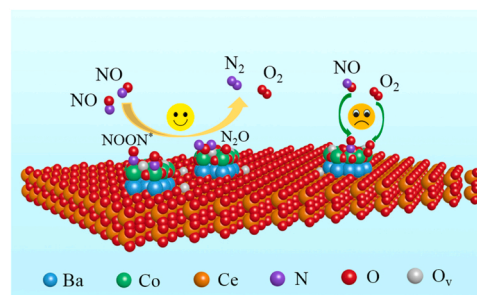


Fig. 9. (a) Optimized structure, (b) Energy profile and (c), (d) Reaction structure of NO direct decomposition.



Scheme 1. The morphology-activity relationship of catalysts.



Scheme 2. Reaction pathways for NO direct decomposition over BCR catalyst.

both Co species and adjacent oxygen vacancies act as active sites, and the decomposition of N<sub>2</sub>O\* intermediate is the RDS. Further based on the isotopic (<sup>18</sup>O<sub>2</sub>) exchange results, the intrinsic effect of adding O<sub>2</sub> highlights that an appropriate amount of lattice oxygen promotes the formation of nitrite species at the initial stage of the reaction. Nevertheless, an excessive amount of O<sub>2</sub> occupies more oxygen vacancies and thus inhibits the NO\* formation and transformation of NO\* into N<sub>2</sub>O\*, due to the competitive adsorption of NO and O<sub>2</sub> on the oxygen vacancies of active sites, inhibiting the NO direct decomposition reaction.

#### CRedit authorship contribution statement

**Lu Wang:** Writing – original draft, Methodology, Investigation. **Gang Wang:** Supervision, Funding acquisition. **Hong Chen:** Validation, Methodology, Investigation. **Cuijuan Zhang:** Validation, Resources, Investigation. **Running Kang:** Writing – original draft, Methodology, Investigation, Formal analysis, Data curation, Conceptualization. **Xuehai Wang:** Writing – review & editing, Resources, Project administration. **Junqin Huang:** Investigation, Data curation. **Sufeng An:** Resources, Investigation, Conceptualization. **Feng Bin:** Validation, Resources, Investigation, Data curation. **Yongdan Li:** Writing – review &

editing, Supervision, Resources, Funding acquisition, Conceptualization.

### Declaration of Competing Interest

The authors declare that they have no known competing financial interests or personal relationships that could have appeared to influence the work reported in this paper.

### Data availability

No data was used for the research described in the article.

### Acknowledgments

The authors gratefully acknowledge the financial support from the International Science and Technology Cooperation Projects (Sinopec. 410920). Running Kang sincerely acknowledge the financial support from the China Scholarship Council (CSC, No. 202004910623), China National Postdoctoral Program for Innovative Talents (No. BX20230380) and The Youth Fund of the State Key Laboratory of High Temperature Gas Dynamics (No.2023QN07). We also sincerely thank for the help of Gen Li (PhD student, DFT calculation and discussion, CSC No. 202208320030), Qianyuan Qiu (PhD student, SEM operation, CSC No. 201906150134) and Penghui Yao (PhD student, catalyst preparation, CSC No. 202006120046), and DFT simulation from CSC-IT Center for Science, Finland, for computational resources.

### Appendix A. Supporting information

Supplementary data associated with this article can be found in the online version at doi:10.1016/j.apcatb.2024.123952.

### References

- A. Tourunen, J. Saastamoinen, H. Nevalainen, Experimental trends of NO in circulating fluidized bed combustion, *Fuel* 88 (2009) 1333–1341.
- R. Kang, J. He, F. Bin, B. Dou, Q. Hao, X. Wei, K. Hui, K.S. Hui, Alkali metal-resistant mechanism for selective catalytic reduction of nitric oxide over  $V_2O_5$ /HWO catalysts, *Fuel* 304 (2021) 121445.
- H. Zhao, X. Chen, A. Bhat, Y. Li, J.W. Schwank, Understanding the chemistry during the preparation of Pd/SSZ-13 for the low-temperature NO adsorption: the role of NH<sub>4</sub>-SSZ-13 support, *Appl. Catal. B: Environ.* 282 (2017) 119611.
- Y. Wu, X. Zhou, T. Mi, B. Hu, J. Liu, Q. Lu, Effect of WO<sub>3</sub> and MoO<sub>3</sub> doping on the interaction mechanism between arsenic oxide and V<sub>2</sub>O<sub>5</sub>-based SCR catalyst: a theoretical account, *Mol. Catal.* 499 (2021) 111317.
- Y. Yang, J. Liu, F. Liu, Z. Wang, J. Ding, H. Huang, Reaction mechanism for NH<sub>3</sub>-SCR of NO<sub>x</sub> over CuMn<sub>2</sub>O<sub>4</sub> catalyst, *Chem. Eng. J.* 316 (2019) 578–587.
- D.D. Chen, Y.L. Yan, A.Q. Guo, V. Rizzotto, H.R. Lei, Z.W. Qiao, H. Liang, M. Jabłońska, X.Q. Jiang, J.X. Jiang, R. Palkovits, P.R. Chen, D.Q. Ye, U. Simon, Mechanistic insights into the promotion of low-temperature NH<sub>3</sub>-SCR catalysis by copper auto-reduction in Cu-zeolites, *Appl. Catal. B: Environ.* 322 (2023) 122118.
- J. Wang, H. Zhao, G. Haller, Y. Li, Recent advances in the selective catalytic reduction of NO<sub>x</sub> with NH<sub>3</sub> on Cu-Chabazite catalysts, *Appl. Catal. B: Environ.* 202 (2021) 346–354.
- J.J. Liu, X.Y. Shi, Y.B. Yu, M.Y. Zhang, D.R. Liu, H. He, Excellent hydrocarbon tolerance of CeO<sub>2</sub>-WO<sub>3</sub>-SnO<sub>2</sub> oxide catalyst for the NH<sub>3</sub>-SCR of NO<sub>x</sub>, *Appl. Catal. B: Environ.* 324 (2023) 122283.
- Y. Zhang, G. Cao, X. Yang, Advances in De-NO<sub>x</sub> methods and catalysts for direct catalytic decomposition of NO: a review, *Energy Fuels* 35 (2021) 6443–6464.
- F. Garin, Mechanism of NO<sub>x</sub> decomposition, *Appl. Catal. A Gen.* 222 (2001) 183–219.
- P. Xie, W.X. Ji, Y. Li, C. Zhang, NO direct decomposition: progress, challenges and opportunities, *Catal. Sci. Technol.* 11 (2021) 374–391.
- R.N. Kang, S.F. An, X.H. Wang, G. Wang, H. Chen, C.J. Zhang, F. Bin, Y.D. Li, Support effect and reaction pathway for NO direct decomposition over CuMn/A (A=ZSM-5, Beta, SSZ-13) catalysts, *Catal. Today* 430 (2024) 114545.
- W.B. Bae, D.Y. Kim, S.W. Byun, S.J. Lee, S.K. Kuk, H.J. Kwon, H.C. Lee, M. J. Hazlett, C. Liu, Y.J. Kim, M. Kim, S.B. Kang, Direct NO decomposition over Rh-supported catalysts for exhaust emission control, *Chem. Eng. J.* 475 (2023) 146005.
- M.S. Jia, R.J. Deng, F. Li, K.W. Xu, Y. Ye, Z.F. Wang, H.L. Yang, X.H. Wang, Solution combustion synthesis of a Y<sub>0.87</sub>Ba<sub>0.13</sub>Zr<sub>0.03</sub>O<sub>1.465</sub> catalyst for highly efficient NO direct decomposition at high temperatures, *Energy Fuels* 37 (2023) 19704–19714.
- S. Royer, D. Duprez, F. Can, X. Courtois, C. Batiot-Dupeyrat, S. Laassiri, H. Alamdari, Perovskites as substitutes of noble metals for heterogeneous catalysis: dream or reality, *Chem. Rev.* 114 (2014) 10292–10368.
- W. Xu, J. Cai, J. Zhou, Y. Ou, W. Long, Z. You, Y. Luo, Highly effective direct decomposition of nitric oxide by microwave catalysis over BaMeO<sub>3</sub> (Me=Mn, Co, Fe) mixed oxides at low temperature under excess oxygen, *ChemCatChem* 8 (2016) 417–425.
- M. Jang, S. Yoon, D. Shin, H. Kim, R. Huang, E. Yang, J.H. Kim, K.S. Lee, K. An, J. W. Han, Boosting, support reducibility and metal dispersion by exposed surface atom control for highly active supported metal catalysts, *ACS Catal.* 12 (2022) 4402–4414.
- Y. Gao, Z. Zhang, Z. Li, W. Huang, Understanding morphology-dependent CuO<sub>x</sub>-CeO<sub>2</sub> interactions from the very beginning, *Chin. J. Catal.* 41 (2020) 1006–1016.
- P. Xie, X. Yong, M. Wei, Y. Li, C. Zhang, High performance catalysts BaCoO<sub>3</sub>-CeO<sub>2</sub> prepared by the one-pot method for NO direct decomposition, *ChemCatChem* 12 (2020) 4297–4303.
- P. Xie, X. Yong, Y. Li, S. Liu, C. Zhang, Tailoring the BaCoO<sub>3</sub>-CeO<sub>2</sub> catalyst for NO direct decomposition: Factors determining catalytic activity, *J. Catal.* 400 (2021) 301–309.
- W. Ji, P. Xie, Y. Li, C. Zhang, Highly efficient NO direct decomposition over BaMnO<sub>3</sub>-CeO<sub>2</sub> composite catalysts, *Appl. Catal. A Gen.* 634 (2022) 118543.
- S. Shin, H. Arakawa, Y. Hatakeyama, K. Ogawa, K. Shimomura, Absorption of NO in the lattice of an oxygen-deficient perovskite SrFeO<sub>3-x</sub> and the infrared spectroscopic study of the system NO-SrFeO<sub>3-x</sub>, *Mater. Res. Bull.* 14 (1979) 633–639.
- Y. Teraoka, T. Harada, S. Kagawa, Reaction mechanism of direct decomposition of nitric oxide over Co- and Mn-based perovskite-type oxides, *J. Chem. Soc. Faraday Trans. 94* (1998) 1887–1891.
- L. Chen, X. Niu, Z. Li, Y. Dong, D. Wang, F. Yuan, Y. Zhu, The effects of BaO on the catalytic activity of La<sub>1.6</sub>Ba<sub>0.4</sub>NiO<sub>4</sub> in direct decomposition of NO, *J. M. Catal. A: Chem.* 423 (2016) 277–284.
- H. Iwakuni, Y. Shinmyou, H. Yano, H. Matsumoto, T. Ishihara, Direct decomposition of NO into N<sub>2</sub> and O<sub>2</sub> on BaMnO<sub>3</sub>-based perovskite oxides, *Appl. Catal. B: Environ.* 74 (2007) 299–306.
- S. Fang, A. Takagaki, M. Watanabe, T. Ishihara, The direct decomposition of NO into N<sub>2</sub> and O<sub>2</sub> over copper doped Ba<sub>3</sub>Y<sub>4</sub>O<sub>9</sub>, *Catal. Sci. Technol.* 10 (2020) 2513–2522.
- S. Tsujimoto, K. Yasuda, T. Masui, N. Imanaka, Effects of Tb and Ba introduction on the reaction mechanism of direct NO decomposition over C-type cubic rare earth oxides based on Y<sub>2</sub>O<sub>3</sub>, *Catal. Sci. Technol.* 3 (2013) 1928–1936.
- P. Sudarsanam, B. Hillary, B. Mallesham, B.G. Rao, M.H. Amin, A. Nafady, A. M. Alsalm, B.M. Reddy, S.K. Bhargava, Designing CuO<sub>x</sub> nanoparticle-decorated CeO<sub>2</sub> nanocubes for catalytic soot oxidation: role of the nanointerface in the catalytic performance of heterostructured nanomaterials, *Langmuir* 32 (2016) 2208–2215.
- Y. Guo, Y. Qin, H. Liu, H. Wang, J. Han, X. Zhu, Q. Ge, CeO<sub>2</sub> facet-dependent surface reactive intermediates and activity during ketonization of propionic acid, *ACS Catal.* 12 (2022) 2998–3012.
- G.K. Reddy, T.C. Peck, C.A. Roberts, CeO<sub>2</sub>-M<sub>x</sub>O<sub>y</sub> (M = Fe, Co, Ni, and Cu)-based oxides for direct NO decomposition, *J. Phys. Chem. C* 123 (2019) 28695–28706.
- J. Ma, G. Jin, J. Gao, Y. Li, L. Dong, M. Huang, Q. Huang, B. Li, Catalytic effect of two-phase intergrowth and coexistence CuO-CeO<sub>2</sub>, *J. Mater. Chem. A* 3 (2015) 24358–24370.
- R. Kang, P. Ma, J. He, H. Li, F. Bin, X. Wei, B. Dou, K.N. Hui, K.S. Hui, Transient, behavior and reaction mechanism of CO catalytic ignition over a CuO-CeO<sub>2</sub> mixed oxide, *Proc. Combust. Inst.* 38 (2021) 6493–6501.
- X. Liao, W. Chu, X. Dai, V. Pitchon, Promoting effect of Fe in preferential oxidation of carbon monoxide reaction (PROX) on Au/CeO<sub>2</sub>, *Appl. Catal. A Gen.* 449 (2012) 131–138.
- W. Zhao, X. Zheng, S. Liang, X. Zheng, L. Shen, F. Liu, Y. Cao, Z. Wei, L. Jiang, Fe-doped  $\gamma$ -Al<sub>2</sub>O<sub>3</sub> porous hollow microspheres for enhanced oxidative desulfurization: facile fabrication and reaction mechanism, *Green Chem.* 20 (2018) 4645–4654.
- S. Liu, Y. Cong, C. Kappenstein, T. Zhang, Effect of zirconium in La(Ba)Zr<sub>1-x</sub>Co<sub>x</sub>O<sub>3- $\delta$</sub>  perovskite catalysts for N<sub>2</sub>O decomposition, *Chin. J. Catal.* 33 (2012) 907.
- K. Chen, B. Chu, Q. Qin, X. Ou, R. Zhao, X. Wei, H. Wu, B. Li, L. Dong, Effect of reduction on NO + CO reaction performance of CuO-Co<sub>3</sub>O<sub>4</sub> symbiotic oxide porous nanosheet and DFT calculation, *Appl. Surf. Sci.* 589 (2022) 153052.
- H. Zhu, Z. Qin, W. Shan, W. Shen, J. Wang, Pd/CeO<sub>2</sub>-TiO<sub>2</sub> catalyst for CO oxidation at low temperature: a TPR study with H<sub>2</sub> and CO as reducing agents, *J. Catal.* 255 (2004) 267–277.
- Z. Zhao, X. Yang, Y. Wu, Comparative study of Nickel-based perovskite-like mixed oxide catalysts for direct decomposition of NO, *Appl. Catal. B: Environ.* 8 (1996) 281–297.
- G.K. Reddy, T.C. Peck, C.A. Roberts, CeO<sub>2</sub>-M<sub>x</sub>O<sub>y</sub> (M = Fe, Co, Ni, and Cu)-based oxides for direct NO decomposition, *J. Phys. Chem. C* 123 (2019) 28695.
- J. Chen, M. Shen, X. Wang, J. Wang, Y. Su, Z. Zhao, Catalytic performance of NO oxidation over LaMeO<sub>3</sub> (Me = Mn, Fe, Co) perovskite prepared by the sol-gel method, *Catal. Commun.* 37 (2013) 105–108.
- T. Ishihara, M. Ando, K. Sada, K. Takiishi, K. Yamada, H. Nishiguchi, Y. Takita, Direct decomposition of NO into N<sub>2</sub> and O<sub>2</sub> over La(Ba)Mn(In)O<sub>3</sub> perovskite oxide, *J. Catal.* 220 (2003) 104–114.
- Y. Li, T.L. Slager, J.N. Armor, Selective reduction of NO<sub>x</sub> by methane on Co-Ferrierites: II. Catalyst characterization, *J. Catal.* 150 (1994) 388–399.
- K. Hadjiivanov, B. Tsyntarski, T. Nikolova, Stability and reactivity of the nitrogen-oxo species formed after NO adsorption and NO+O<sub>2</sub> coadsorption on Co-ZSM-5: an FTIR spectroscopic study, *Phys. Chem. Chem. Phys.* 1 (1999) 4521–4528.

- [44] K.A. Windhorst, J.H. Lunsford, Structure and reactivity of cobalt-nitrosyl complexes in Y-type zeolites, *J. Am. Chem. Soc.* 97 (1975) 1407–1412.
- [45] B. Djonev, B. Tsyntsarski, D. Klissurski, K. Hadjiivanov, IR spectroscopic study of NO<sub>x</sub> adsorption and NO<sub>x</sub>-O<sub>2</sub> coadsorption on Co<sup>2+</sup>/SiO<sub>2</sub> catalysts, *J. Chem. Soc. Faraday Trans.* 93 (1997) 4055–4063.
- [46] A. Martínez-Arias, J. Soria, J.C. Conesa, X.L. Seoane, A. Arcoya, R. Cataluña, NO reaction at surface oxygen vacancies generated in cerium oxide, *J. Chem. Soc. Faraday Trans.* 91 (1995) 1679–1687.
- [47] D. Pozdnyakov, V. Filimonov, Infrared spectroscopic study of the chemisorption of nitric oxide and nitrogen dioxide on metal oxides, *Kinet. Katal.* 14 (1973) 760–766.
- [48] S. Xie, M.P. Rosynek, J.H. Lunsford, Catalytic reactions of NO over 0–7 mol % Ba/MgO catalysts: I. the direct decomposition of NO, *J. Catal.* 188 (1999) 24–31.
- [49] J.S.J. Hargreaves, S.D. Jackson, G. Webb, *Isotopes on Heterogeneous catalysis. Catalytic Science Series*, 4.
- [50] Z. Pan, Y. Li, Y. Zhao, C. Zhang, H. Chen, Bulk phase charge transfer in focus – and in sequential along with surface steps, *Catal. Today* 364 (2021) 2–6.
- [51] D. Damma, T. Boningari, P.R. Ettireddy, B.M. Reddy, P.G. Smirniotis, Direct decomposition of NO<sub>x</sub> over TiO<sub>2</sub> supported transition metal oxides at low temperatures, *Ind. Eng. Chem. Res.* 57 (2018) 16615–16621.
- [52] J. Ndalamo, A.F. Mulaba-Bafubandi, B.B. Mamba, UV/visible spectroscopic analysis of Co<sup>3+</sup> and Co<sup>2+</sup> during the dissolution of cobalt from mixed Co-Cu oxidized ores, *Int. J. Miner. Metall. Mater.* 18 (2010) 260–269.
- [53] J.D. Cafun, K.O. Kvashnina, E. Casals, V.F. Puentes, P. Glatzel, Absence of Ce<sup>3+</sup> sites in chemically active colloidal ceria nanoparticles, *ACS Nano* 7 (2013) 10726–10732.
- [54] R.T. Tung, Recent advances in Schottky barrier concepts, *Mater. Sci. Eng. R.* 35 (2001) 1–138.
- [55] J. Wang, T. Fu, F. Meng, D. Zhao, S.S.C. Chuang, Z. Li, Highly active catalysis of methanol oxidative carbonylation over nano Cu<sub>2</sub>O supported on micropore-rich mesoporous carbon, *Appl. Catal. B: Environ.* 303 (2022) 120890.
- [56] R.N. Kang, J.Q. Huang, F. Bin, Z.H. Teng, X.L. Wei, B.J. Dou, S. Kasipandi, Evolution behavior and active oxygen quantification of reaction mechanism on cube Cu<sub>2</sub>O for CO self-sustained catalytic combustion and chemical-looping combustion, *Appl. Catal. B: Environ.* 310 (2022) 121296.
- [57] A. Chen, X. Yu, Y. Zhou, S. Miao, Y. Li, S. Kuld, J. Sehested, J. Liu, T. Aoki, S. Hong, M.F. Camellone, S. Fabris, J. Ning, C. Jin, C. Yang, A. Nefedov, C. Wöll, Y. Wang, W. Shen, Structure of the catalytically active copper–ceria interfacial perimeter, *Nat. Catal.* 2 (2019) 334–341.
- [58] S.D. Senanayake, D. Stacchiola, J.A. Rodriguez, Unique properties of ceria nanoparticles supported on metals: novel inverse ceria/copper catalysts for CO oxidation and the water–gas shift reaction, *Acc. Chem. Res.* 46 (2013) 1702–1711.
- [59] T.E. James, S.L. Hemmingson, C.T. Campbell, Energy of supported metal catalysts: from single atoms to large metal nanoparticles, *ACS Catal.* 5 (2015) 5673–5678.
- [60] X.H. Zheng, Y.L. Li, L.Y. Zhang, L.J. Shen, Y.H. Xiao, Y.F. Zhang, C. Au, L.L. Jiang, Insight into the effect of morphology on catalytic performance of porous CeO<sub>2</sub> nanocrystals for H<sub>2</sub>S selective oxidation, *Appl. Catal. B: Environ.* 252 (2019) 98–110.
- [61] M. Haneda, Y. Kintaichi, H. Hamada, Reaction mechanism of NO decomposition over alkali metal-doped cobalt oxide catalysts, *Appl. Catal. B: Environ.* 55 (2005) 169–175.